CHAPTER 4

RECOVERY OF THREE-INTEGRAL GALAXY MODELS

ABSTRACT

We construct axisymmetric and triaxial galaxy models with a phase-space distribution function that depends on linear combinations of the three exact integrals of motion for a separable potential. These Abel models, first introduced by Dejonghe & Laurent and subsequently extended by Mathieu & Dejonghe, are the axisymmetric and triaxial generalizations of the well-known spherical Osipkov–Merritt models. Their density and higher velocity moments can be calculated efficiently and we show that they capture much of the rich internal dynamics of early-type galaxies. We use these models to mimic the high-quality two-dimensional kinematic observations that are obtained with integral-field spectrographs such as SAURON. We fit the simulated observations with axisymmetric and triaxial dynamical models obtained with our numerical implementation of Schwarzschild's orbit-superposition method, while varying the viewing direction and the mass-to-light ratio. We find that Schwarzschild's method is able to recover the internal dynamical structure of early-type galaxies and to accurate determine the mass-to-light ratio, but additional information is needed to constrain better the viewing direction.

1   INTRODUCTION

THE equilibrium state of a collisionless stellar system such as an elliptical or lenticular galaxy is completely described by its distribution function (DF) in the six-dimensional phase space of positions and velocities. The recovery of the DF from observations is difficult, as for galaxies other than our own, we can usually only measure the projected surface brightness and the line-of-sight velocity distribution of the integrated light as a function of position on the plane of the sky. Moreover, we generally do not know the intrinsic shape of the galaxy, nor the viewing direction, or the contribution to the gravitational potential provided by a supermassive central black hole and/or an extended halo of dark matter. By Jeans (1915) theorem, the DF is a function of the isolating integrals of motion admitted by the potential, but it is not evident how to take advantage of this property other than for the limiting case of spherical systems. Orbits in axisymmetric geometry have two exact integrals of motion, the energy E and the angular momentum component L_z parallel to the symmetry axis, but the third effective or non-classical integral I_3 obeyed by all regular orbits is generally not known in closed form. In stationary triaxial geometry E is conserved, but regular orbits now have two additional effective integrals of motion, I_2 and I_3, which are not known explicitly.

Schwarzschild (1979, 1982) devised a numerical method which sidesteps our ignorance about the non-classical integrals of motion. It allows for an arbitrary gravitational potential, which may include contributions from dark components, integrates the equations of motion for a representative library of orbits, computes the density distribution of each orbit, and then determines the orbital weights such that the combined orbital densities reproduce the density of the system. The best-fitting orbital weights represent the DF (cf. Vandervoort 1984). Pfenniger (1984) and Richstone & Tremaine (1984) included kinematic moments in this method, and Rix et al. (1997) showed how to include the line-of-sight velocity profiles. A number of groups have developed independent numerical implementations of Schwarzschild's method for axisymmetric geometry which fit the projected surface brightness and line-of-sight velocity distributions of early-type galaxies in detail (van der Marel et al. 1998; Cretton et al. 1999; Gebhardt et al. 2000, Cappellari et al. 2002; Valluri, Merritt & Emsellem 2004; Thomas et al. 2004). Applications include the determination of central black hole masses (see also van der Marel et al. 1997; Cretton & van den Bosch 1999; Verolme et al. 2002; Gebhardt et al. 2003; Copin, Cretton & Emsellem 2004), very accurate global dynamical mass-to-light ratios (Cappellari et al. 2005), as well as dark matter profiles as a function of radius (Cretton, Rix & de Zeeuw 2000; Thomas et al. 2005), and recovery of the DF (Krajnović et al. 2005). Finally, van de Ven et al. (2005) included proper motion measurements in order to model nearby globular clusters, and Verolme et al. (2003) and van den Bosch et al. (2006) describe an extension to triaxial geometry that includes all line-of-sight kinematics.

Although Schwarzschild models have significantly increased our understanding of the dynamical structure and evolution of early-type galaxies, questions remain about the uniqueness and the accuracy with which they are able to recover the global parameters as well as the internal dynamics of these galaxies. Many tests have been done to establish how the axisymmetric code recovers known input models, but these generally have been limited to spherical geometry or to an input axisymmetric DF that is a function of E and L_z only (van der Marel et al. 1998; Cretton et al. 1999;

Verolme & de Zeeuw 2002; Valluri et al. 2004; Cretton & Emsellem 2004; Thomas et al. 2004; Krajnović et al. 2005). The code for triaxial geometry so far has been tested for densities consistent with a DF that depends on E only.

One could construct a numerical galaxy model with Schwarzschild's method itself, compute the observables, and then use these as input for the code and determine how well it recovers the input model. This is useful, but does not provide a fully independent test of the software. An alternative is to consider the special family of models with gravitational potential of Stäckel form, for which all three integrals of motion are exact and known explicitly. The potentials of these models have a core rather than a central cusp, so the models cannot include a central black hole, and are inadequate for describing galactic nuclei. However, they can be constructed for a large range of axis ratios (Statler 1987), and their observed kinematic properties are as rich as those seen in the main body of early-type galaxies (Statler 1991, 1994; Arnold, de Zeeuw & Hunter 1994).

A small number of analytic DFs have been constructed for triaxial separable models. The 'thin-orbit' models (Hunter & de Zeeuw 1992) have the maximum possible streaming motions, but their DF contains delta functions, and they are therefore not particularly useful for a test of general-purpose numerical machinery. Dejonghe & Laurent (1991, hereafter DL91) constructed separable triaxial models in which the DF depends on a single parameter $S = E + wI_2 + uI_3$, which is a linear combination of the three exact integrals E, I_2 and I_3 admitted by these potentials, and is quadratic in the velocity components. For a given radial density profile, the DF follows by simple inversion of an Abel integral equation. These so-called Abel models have no net mean streaming motions, and are the axisymmetric and triaxial generalizations of the well-known spherical Osipkov–Merritt models (Osipkov 1979; Merritt 1985), for which the observables can be calculated easily (Carollo, de Zeeuw & van der Marel 1995). Mathieu & Dejonghe (1999, hereafter MD99) generalized the results of DL91 by including two families of DF components with net internal mean motions around the long and the short axis, respectively, and compared the resulting models with observations of Centaurus A. Although the Abel character of the non-rotating components is no longer conserved, the expressions for the velocity moments in these more general models can still be evaluated in a straightforward way. When the entire DF depends on the same single variable S the famous ellipsoidal hypothesis (e.g., Eddington 1915; Chandrasekhar 1940) applies, so that self-consistency is only possible in the spherical case (Eddington 1916; Camm 1941). This does not hold for Abel models with a DF that is a sum of components for which the variable S has different values of the parameters w and u. Such multi-component Abel models can provide (nearly) self-consistent models with a large variety of shapes and dynamics.

Here, we construct axisymmetric and triaxial Abel models to test our numerical implementation of Schwarzschild's method. We assume a convenient form for the gravitational potential, and construct the DF that reproduces a realistic surface brightness distribution. We compute the resulting intrinsic moments of the models, and then derive two-dimensional maps of the observed kinematics. We show that, despite the simple form of the DF, these models display the large variety of features observed in early-type galaxies with integral-field spectrographs such as SAURON (Emsellem et al. 2004). We fit axisymmetric and triaxial Schwarzschild dynamical models to the resulting simulated observables to investigate the accuracy of the recovery of the internal dynamics and the DF, and determine how well the intrinsic shape, orientation

and mass-to-light ratio are constrained. The oblate limiting case provides a new and convenient three-integral test for the axisymmetric code. We find that Schwarzschild's method is able to recover the internal dynamical structure of early-type galaxies and is able to accurately measure the mass-to-light ratio, but the viewing angles are only weakly constrained.

This chapter is organized as follows. In Section 2 we summarize the properties of the triaxial Abel models of DL91 and MD99 in a form which facilitates their numerical implementation. In Section 3 we describe the conversion to observables, and in Section 4 we construct a specific triaxial galaxy model. In Section 5 we consider the axisymmetric limit and construct a three-integral oblate galaxy model. In Section 6 and 7 we fit the observables of both Abel models with our numerical Schwarzschild models, and investigate how well the intrinsic moments and three-integral DF as well as the values of the global parameters are recovered. We summarize our conclusions in Section 8. In Appendix A we describe the simpler Abel models for the elliptic disk, large distance and spherical limit, and link them to the classical Osipkov–Merritt solutions for spheres. Readers who are mainly interested in the tests of the Schwarzschild method may skip Sections 2–5 on the first reading.

2   TRIAXIAL ABEL MODELS

The triaxial Abel models introduced by DL91 have gravitational potentials of Stäckel form, for which the equations of motion separate in confocal ellipsoidal coordinates. We briefly describe these potentials, and refer for further details to de Zeeuw (1985a). We then make a specific choice for the DF, for which the velocity moments simplify.

2.1   STÄCKEL POTENTIALS

We define confocal ellipsoidal coordinates (λ, μ, ν) as the three roots for τ of

$$\frac{x^2}{\tau + \alpha} + \frac{y^2}{\tau + \beta} + \frac{z^2}{\tau + \gamma} = 1, \tag{2.1}$$

with (x, y, z) the usual Cartesian coordinates, and with constants α, β and γ such that $-\gamma \leq \nu \leq -\beta \leq \mu \leq -\alpha \leq \lambda$. From the inverse relations

$$x^2 = \frac{(\lambda + \alpha)(\mu + \alpha)(\nu + \alpha)}{(\alpha - \beta)(\alpha - \gamma)}, \tag{2.2}$$

and similarly for y^2 and z^2 by cyclic permutation of $\alpha \to \beta \to \gamma \to \alpha$, it follows that a combination (λ, μ, ν) generally corresponds to eight different points $(\pm x, \pm y, \pm z)$. In these coordinates, the Stäckel potentials have the following form (Weinacht 1924)

$$V_S(\lambda, \mu, \nu) = \frac{U(\lambda)}{(\lambda - \mu)(\lambda - \nu)} + \frac{U(\mu)}{(\mu - \nu)(\mu - \lambda)} + \frac{U(\nu)}{(\nu - \lambda)(\nu - \mu)}, \tag{2.3}$$

where $U(\tau)$ is an arbitrary smooth function ($\tau = \lambda, \mu, \nu$). The right-hand side of eq. (2.3) can be recognized as the second order divided difference of $U(\tau)$. Henceforth, we denote it with the customary expression $U[\lambda, \mu, \nu]$, which is symmetric in its arguments (see Hunter & de Zeeuw 1992, eqs 2.1–2.3, 2.13 and 2.14). Addition of an arbitrary linear function of τ to $U(\tau)$ does not change V_S.

The density ρ_S that corresponds to V_S can be found from Poisson's equation

$$4\pi G \rho_S(\lambda, \mu, \nu) = \nabla^2 V_S(\lambda, \mu, \nu), \tag{2.4}$$

or alternatively by application of Kuzmin's (1973) formula (see de Zeeuw 1985b). This formula shows that, once we have chosen the confocal coordinate system and the density along the short axis, the mass model is fixed everywhere by the requirement of separability[1]. For centrally concentrated mass models, V_S has the x-axis as long-axis and the z-axis as short-axis. In most cases this is also true for the associated density (de Zeeuw, Peletier & Franx 1986).

2.2   ORBITAL STRUCTURE

The Hamilton-Jacobi equation separates in (λ, μ, ν) for the potentials (2.3), so that every orbit has three exact integrals of motion (cf. de Zeeuw & Lynden-Bell 1985)

$$
\begin{aligned}
E &= \tfrac{1}{2}\left(v_x^2 + v_y^2 + v_z^2\right) + U[\lambda, \mu, \nu], \\
I_2 &= \tfrac{1}{2}TL_y^2 + \tfrac{1}{2}L_z^2 + \tfrac{1}{2}(\alpha - \beta)v_x^2 - (\beta - \alpha)x^2 U[\lambda, \mu, \nu, -\alpha], \\
I_3 &= \tfrac{1}{2}L_x^2 + \tfrac{1}{2}(1 - T)L_y^2 + \tfrac{1}{2}(\gamma - \beta)v_z^2 + (\gamma - \beta)z^2 U[\lambda, \mu, \nu, -\gamma],
\end{aligned}
\tag{2.5}
$$

where v_x, v_y and v_z are the velocity components in the Cartesian coordinate system, and from $L_x = yv_z - zv_y$, the component of the angular momentum vector parallel to the x-axis, L_y and L_z follow by cyclic permutation of $x \to y \to z \to x$ and $v_x \to v_y \to v_z \to v_x$. Furthermore, T is a triaxiality parameter defined as

$$
T = (\beta - \alpha)/(\gamma - \alpha),
\tag{2.6}
$$

and $U[\lambda, \mu, \nu, \sigma]$ is the third-order divided difference of $U(\tau)$. All models for which $U'''(\tau) > 0$, have similar orbital structure and support four families of regular orbits: boxes (B) with no net rotation, inner (I) and outer (O) long-axis tubes with net rotation around the x-axis, and short-axis (S) tubes with net rotation around the z-axis (Kuzmin 1973; de Zeeuw 1985a; Hunter & de Zeeuw 1992).

According to Jeans (1915) theorem the phase-space distribution function (DF) is a function $f(E, I_2, I_3)$ of the isolating integrals of motion (cf. Lynden-Bell 1962; Binney 1982). The velocity moments of the DF are defined as

$$
\mu_{lmn}(\lambda, \mu, \nu) = \iiint v_\lambda^l v_\mu^m v_\nu^n f(E, I_2, I_3) \, \mathrm{d}v_\lambda \, \mathrm{d}v_\mu \, \mathrm{d}v_\nu,
\tag{2.7}
$$

where l, m and n are non-negative integers, and v_λ, v_μ and v_ν are the velocity components in the confocal ellipsoidal coordinate system. Many of the velocity moments vanish due to the symmetry of the orbits in these coordinates. The zeroth-order velocity moment is the mass density that corresponds to the DF

$$
\rho_\star(\lambda, \mu, \nu) = \mu_{000}(\lambda, \mu, \nu).
\tag{2.8}
$$

In self-consistent models, $\rho_\star$ must equal ρ_S given in eq. (2.4), the mass density that is related to the potential V_S by Poisson's equation.

---

[1]A third method for the calculation of the density is to use $\rho_S = H[\lambda, \lambda, \mu, \mu, \nu, \nu]$, where the fifth-order divided difference is of the function $H(\tau) = 4a(\tau)U'(\tau) - 2a'(\tau)U(\tau)$ with $a(\tau) = (\tau + \alpha)(\tau + \beta)(\tau + \gamma)$ and $U(\tau)$ defines the potential as in eq. (2.3). This result was obtained by Hunter in 1989 (priv. comm.), and by Mathieu & Dejonghe (1996). Similar expressions exist for the related families of potential-density pairs introduced in de Zeeuw & Pfenniger (1988).

2.3   Abel distribution function

Following DL91, we choose the DF to be a function of the three integrals of motion E, I_2 and I_3 as given in eq. (2.5) through one variable

$$f(E, I_2, I_3) = f(S), \quad \text{with} \quad S = -E + w\,I_2 + u\,I_3, \tag{2.9}$$

and w and u are two parameters[2]. This choice for the DF is equivalent to the celebrated ellipsoidal hypothesis (e.g., Eddington 1915; Chandrasekhar 1940). Self-consistency is only possible in the spherical case (Eddington 1916; Camm 1941). On the other hand, these DFs can produce realistic (luminous) mass densities $\rho_\star$, which differ from the (total) mass density ρ_S, as in galaxies with dark matter (but see § 3.4 below when we combine DFs of the form [2.9] with different values for w and u.)

   DL91 and MD99 divided the DF into three types of components. The non-rotating (NR) type is made of box orbits and tube orbits with both senses of rotation populated equally. The two rotating types, LR and SR, consist of tube orbits, and have net rotation around either the long axis or the short axis.

2.3.1   Velocity moments

Due to the choice (2.9) of the DF, the general expression (2.7) for the velocity moments can be simplified, as shown by DL91 for the non-rotating component and by MD99 for the rotating components. We recast their results into a different form to facilitate the numerical implementation. The resulting velocity moments are given by

$$\mu_{lmn}(\lambda, \mu, \nu) = \sqrt{\frac{2^{l+m+n+3}}{H_{\mu\nu}^{l+1} H_{\nu\lambda}^{m+1} H_{\lambda\mu}^{n+1}}} \int_{S_{\min}}^{S_{\max}} T_{lmn} \left[S_{\text{top}}(\lambda, \mu, \nu) - S\right]^{(l+m+n+1)/2} f(S)\,\mathrm{d}S, \tag{2.10}$$

and set to zero at positions for which $S_{\max} \leq S_{\min}$. The terms $H_{\mu\nu}$, $H_{\nu\lambda}$ and $H_{\lambda\mu}$ in the square root in front of the integral are defined as

$$H_{\sigma\tau} = 1 + \frac{(\sigma + \alpha)(\tau + \alpha)}{\gamma - \alpha}\,w + \frac{(\sigma + \gamma)(\tau + \gamma)}{\alpha - \gamma}\,u, \tag{2.11}$$

with $\sigma, \tau = \lambda, \mu, \nu$. Orbits are confined to the region of space for which all three terms are non-negative. In general, this condition will not be satisfied for all points, so that the Abel components have finite extent. From the requirement that at least the origin $(\lambda, \mu, \nu) = (-\alpha, -\beta, -\gamma)$ should be included, we find the following limits on w and u

$$w \geq -\frac{1}{\beta - \alpha} \quad \text{and} \quad u \leq \frac{1}{\gamma - \beta}. \tag{2.12}$$

The factor T_{lmn} in the integrand as well as the upper limit $S_{\max}$ of the integral are different for each of the three Abel component types NR, LR and SR, and are discussed in §§ 2.3.2–2.3.4 below. The lower limit of the integral $S_{\min}$ has to be at least as large as the smallest value possible for the variable S. This limiting value S_{lim} depends on the choice of the DF parameters w and u (eq. 2.9), as is shown in Fig. 2 (cf. Fig. 7 of DL91). The boundaries follow from (2.12) and the separatrices L_1 and L_2 are given by

$$L_1 : w = \frac{u^2\,U(\frac{1}{u} - \gamma)}{(\beta - \alpha)[1 - (\gamma - \alpha)\,u]}, \quad L_2 : w = \frac{u}{1 - (\gamma - \alpha)\,u}. \tag{2.13}$$

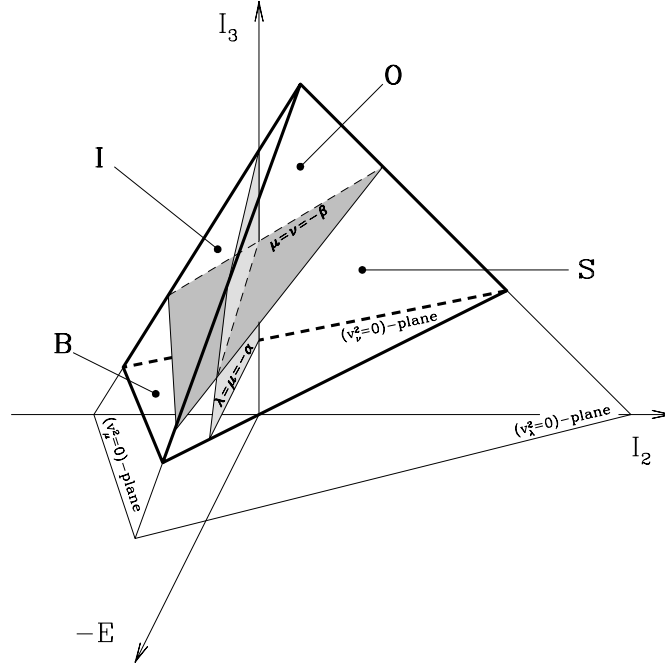[2]In contrast with DL91 and MD99, we choose $V_S \leq 0$ and $E \leq 0$, consistent with e.g. de Zeeuw (1985a).

FIGURE 1 — *The tetrahedron shows all accessible points in integral space (E, I_2, I_3) for a given position (λ, μ, ν). The tetrahedron is bounded by the planes for which $v_\lambda^2 = 0$, $v_\mu^2 = 0$, $v_\nu^2 = 0$ and $E = 0$, respectively. The two shaded planes, which are given by $v_\lambda^2 = v_\mu^2 = 0$ at $\lambda = \mu = -\alpha$ and $v_\mu^2 = v_\nu^2 = 0$ at $\mu = \nu = -\beta$, divide the tetrahedron into the parts corresponding to the four general orbit families in a triaxial separable potential: box (B) orbits, inner (I) and outer (O) long-axis tube orbits and short-axis (S) tube orbits.*

At a given position (λ, μ, ν), orbits with different values of the integrals of motion E, I_2 and I_3, and hence different values of S, can contribute to the integral (2.10). The restriction to bound orbits ($E \leq 0$) together with the requirement that v_λ^2, v_μ^2 and v_ν^2 all three have to be non-negative determines the part of the integral space that is accessible by orbits that go through (λ, μ, ν). An example of the resulting tetrahedron in the (E, I_2, I_3)-space is shown in Fig. 1 (cf. Fig. 1 of MD99). The largest possible value of S is given by the top of this tetrahedron

$$S_{\text{top}}(\lambda, \mu, \nu) = -U[\lambda, \mu, \nu] \; - \; w \, \frac{(\lambda + \alpha)(\mu + \alpha)(\nu + \alpha)}{\gamma - \alpha} \, U[\lambda, \mu, \nu, -\alpha]$$
$$- \; u \, \frac{(\lambda + \gamma)(\mu + \gamma)(\nu + \gamma)}{\alpha - \gamma} \, U[\lambda, \mu, \nu, -\gamma], \qquad (2.14)$$

which is thus a function of the position (λ, μ, ν). At the origin $S_{\text{top}}(-\alpha, -\beta, -\gamma) = U[-\alpha, -\beta, -\gamma]$, which is the central value of the potential V_S. In what follows, we normalize V_S by setting $U[-\alpha, -\beta, -\gamma] = -1$, so that $0 \leq S_{\text{top}} \leq 1$.

2.3.2 Non-rotating components (NR)

Since the non-rotating component type can exist everywhere in the accessible integral space (the tetrahedron in Fig. 1), we simply have that $S_{\text{max}} = S_{\text{top}}(\lambda, \mu, \nu)$. Spatially the
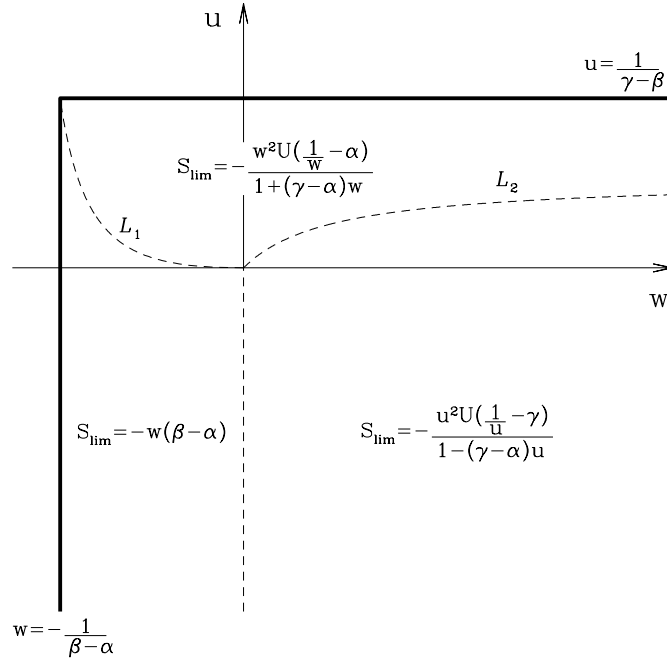
FIGURE 2 — *The limiting value S_{lim} of the variable $S = -E + w\, I_2 + u\, I_3$ as function of the parameters w and u. The physical region is bounded by the relations (2.12), indicated by the thick solid lines. The dashed curves divide this region into three parts, each with a different expression for S_{lim}. The relations for the separatrices L_1 and L_2 are given in eq. (2.13).*

NR components are thus bounded by the surface $S_{\mathrm{top}}(\lambda, \mu, \nu) = S_{\mathrm{min}}$.

The factor T_{lmn} follows from the cross section of the S-plane within the tetrahedron and can be written in compact form as (cf. DL91)

$$T_{lmn}^{\mathrm{NR}} = B(\tfrac{l+1}{2}, \tfrac{m+1}{2}, \tfrac{n+1}{2}),\tag{2.15}$$

where B is the beta function of three variables[3]. Since T_{lmn}^{NR} is independent of S it can be taken out of the integral, which then becomes of Abel form. Unfortunately, the inversion of eq. (2.10) for any chosen moment $\mu_{lmn}(\lambda, \mu, \nu)$, including the case $l = m = n = 0$, is generally impossible, as the left-hand side is a function of three variables, while the DF depends on only one variable, S. The density $\rho_\star$ specified along any given curve will define a different $f(S)$. A case of particular interest is to choose the density along the short axis to be $\rho_\star(0, 0, z) = \rho_S(0, 0, z)$. This defines a unique $f(S)$, and hence gives $\rho_\star$ everywhere. Kuzmin's formula applied to $\rho_S(0, 0, z)$ similarly defines the density ρ_S everywhere. For single Abel DF components these will not be the same, except in the spherical limit (see Appendix A.3)

Since the orbits have no net rotation, the velocity moments μ_{lmn}^{NR} are only non-zero when l, m and n are all three even, and vanish in all other cases.

---

[3]The beta function of k variables is defined in terms of the complete gamma function Γ as $B(\beta_1, \ldots, \beta_k) = \Gamma(\beta_1) \cdots \Gamma(\beta_k)/\Gamma(\beta_1 + \cdots + \beta_k)$.

2.3.3 Long-axis rotating components (LR)

The long-axis rotating component type only exists in the part of the integral space that is accessible by the (inner and outer) long-axis tube orbits. Within the tetrahedron for all orbits this is the region for which $v_\nu^2 \geq 0$ at $\nu = -\beta$. It follows that $S_{\max} = S_{\text{top}}(\lambda, \mu, -\beta) \leq S_{\text{top}}(\lambda, \mu, \nu)$, so that the spatial extent of the LR components is generally smaller than the NR components.

The term T_{lmn} follows from the cross section of the S-plane within the tetrahedron *and* with the above boundary plane $v_\nu^2 = 0$ at $\nu = -\beta$, resulting in

$$T_{lmn}^{\text{LR}} = \frac{(-2)^{(l+m+4)/2} \sqrt{a_0^{l+1} b_0^{m+1}} \, \mathcal{M}_0^{\text{LR}}}{(s+1)(s-1)\dots(s+1-(l+m))}, \tag{2.16}$$

with $s = l + m + n$, the parameters a_0 and b_0 defined as

$$a_0 = \frac{(\lambda + \beta) \, H_{\mu\nu} \, [S_{\text{top}}(\lambda, \mu, -\beta) - S]}{(\lambda - \nu) \, H_{\mu(-\beta)} \, [S_{\text{top}}(\lambda, \mu, \nu) - S]}, \quad b_0 = \frac{(\mu + \beta) \, H_{\nu\lambda} \, [S_{\text{top}}(\lambda, \mu, -\beta) - S]}{(\mu - \nu) \, H_{(-\beta)\lambda} \, [S_{\text{top}}(\lambda, \mu, \nu) - S]}, \tag{2.17}$$

and

$$\mathcal{M}_0^{\text{LR}} = \begin{cases} \mathcal{M}(s, \frac{l}{2}, \frac{m}{2}; a_0, b_0, \frac{\pi}{2}), & a_0 \leq b_0, \\ \mathcal{M}(s, \frac{m}{2}, \frac{l}{2}; b_0, a_0, \frac{\pi}{2}), & a_0 > b_0. \end{cases} \tag{2.18}$$

The function $\mathcal{M}$ is defined in Appendix B, where we evaluate it in terms of elementary functions (odd s) and elliptic integrals (even s).

The orbits have net rotation around the long axis, but the motion parallel to the intermediate axis and short axis cancels. As a result, the velocity moments μ_{lmn}^{LR} vanish when l or m are odd. To invert the net rotation around the long-axis, μ_{lmn}^{LR} has to be multiplied with $(-1)^n$, i.e. the non-zero odd velocity moments have opposite sign.

2.3.4 Short-axis rotating components (SR)

The short-axis component type reaches the part of integral space accessible by the short-axis tube orbits. Within the tetrahedron for all orbits this is the region for which $v_\mu^2 \geq 0$ both at $\mu = -\beta$ and $\mu = -\alpha$ (Fig. 1). The latter requirement is equivalent to $I_2 \geq 0$. In this case, $S_{\max} = S_{\text{top}}(\lambda, -\alpha, \nu) \leq S_{\text{top}}(\lambda, \mu, \nu)$, and the spatial extent of the SR components is generally smaller than the NR components.

The form of the term T_{lmn} depends on the cross section of the S-plane within the tetrahedron and with the above two boundary planes. It is given by

$$T_{lmn}^{\text{SR}} = \frac{(-2)^{(l+n+4)/2} \sum_{i=1}^{2} \sqrt{a_i^{l+1} b_i^{n+1}} \, \mathcal{M}_i^{\text{SR}}}{(s+1)(s-1)\dots(s+1-(l+n))}. \tag{2.19}$$

The parameters a_1 and b_1 follow from a_0 and b_0 defined in (2.17) by interchanging $\nu \leftrightarrow \mu$, and in turn a_2 and b_2 follow from a_1 and b_1 by interchanging $\beta \leftrightarrow \alpha$. For the terms $\mathcal{M}_i^{\text{SR}}$ we have two possibilities, I and II,

$$\mathcal{M}_{\text{I}}^{\text{SR}} = \begin{cases} \mathcal{M}(s, \frac{l}{2}, \frac{n}{2}; a_{\text{I}}, b_{\text{I}}, \theta_{\text{I}}), & a_{\text{I}} \leq b_{\text{I}}, \\ \mathcal{M}(s, \frac{n}{2}, \frac{l}{2}; b_{\text{I}}, a_{\text{I}}, \frac{\pi}{2}) - \mathcal{M}(s, \frac{n}{2}, \frac{l}{2}; b_{\text{I}}, a_{\text{I}}, \frac{\pi}{2} - \theta_{\text{I}}), & a_{\text{I}} > b_{\text{I}}, \end{cases} \tag{2.20}$$

$$\mathcal{M}_{\text{II}}^{\text{SR}} = \begin{cases} \mathcal{M}(s, \frac{l}{2}, \frac{n}{2}; a_{\text{II}}, b_{\text{II}}, \frac{\pi}{2}) - \mathcal{M}(s, \frac{l}{2}, \frac{n}{2}; a_{\text{II}}, b_{\text{II}}, \theta_{\text{II}}), & a_{\text{II}} \leq b_{\text{II}}, \\ \mathcal{M}(s, \frac{n}{2}, \frac{l}{2}; b_{\text{II}}, a_{\text{II}}, \frac{\pi}{2} - \theta_{\text{II}}), & a_{\text{II}} > b_{\text{II}}, \end{cases} \tag{2.21}$$

where $\mathcal{M}$ is given in Appendix B, and θ_{I} and θ_{II} follow from

$$\tan^2 \theta_{\mathrm{I}} = \frac{b_{\mathrm{II}} (a_{\mathrm{I}} - a_{\mathrm{II}})}{a_{\mathrm{II}} (b_{\mathrm{II}} - b_{\mathrm{I}})} \quad \text{and} \quad \tan^2 \theta_{\mathrm{II}} = \frac{b_{\mathrm{I}} (a_{\mathrm{II}} - a_{\mathrm{I}})}{a_{\mathrm{I}} (b_{\mathrm{I}} - b_{\mathrm{II}})}. \tag{2.22}$$

For the assignment of the labels I and II, we discriminate between four cases

$$\begin{aligned}
a_1 \leq a_2, \quad b_1 \geq b_2 \quad &: \quad \mathrm{I} \to 1, \quad \mathrm{II} \to 2, \\
a_1 \geq a_2, \quad b_1 \leq b_2 \quad &: \quad \mathrm{I} \to 2, \quad \mathrm{II} \to 1, \\
a_1 \leq a_2, \quad b_1 \leq b_2 \quad &: \quad \mathrm{I} \to 1, \theta_{\mathrm{I}} = \pi/2, \quad C_2^{\mathrm{SR}} = 0, \\
a_1 \geq a_2, \quad b_1 \geq b_2 \quad &: \quad \mathrm{I} \to 2, \theta_{\mathrm{I}} = \pi/2, \quad C_1^{\mathrm{SR}} = 0.
\end{aligned} \tag{2.23}$$

The orbits only have net rotation around the short axis, so that the velocity moments μ_{lmn}^{SR} vanish when l or n are odd. Multiplying μ_{lmn}^{SR} with $(-1)^m$ results in net rotation around the short axis in the opposite direction.

3   OBSERVABLES

We now describe how to convert the intrinsic velocity moments $\mu_{lmn}(\lambda, \mu, \nu)$ to observable quantities on the plane of the sky: the surface brightness (SB) and the mean line-of-sight velocity V, velocity dispersion σ, as well as higher-order moments of the line-of-sight velocity distribution.

3.1   FROM INTRINSIC TO OBSERVER'S COORDINATE SYSTEM

In order to calculate the projected velocity moments, we introduce a new Cartesian coordinate system (x'', y'', z''), with x'' and y'' in the plane of the sky and the z''-axis along the line-of-sight. Choosing the x''-axis in the (x, y)-plane of the intrinsic coordinate system (cf. de Zeeuw & Franx 1989 and their Fig. 2), the transformation between both coordinate systems is known once two viewing angles, the polar angle ϑ and azimuthal angle φ, are specified. The intrinsic z-axis projects onto the y''-axis, which for an axisymmetric galaxy model aligns with the short axis of the projected surface density Σ. However, for a triaxial galaxy model the y''-axis in general lies at an angle ψ with respect to the short axis of Σ. This misalignment ψ can be expressed in terms of the viewing angles ϑ and φ and the triaxiality parameter T (defined in eq. 2.6) as follows (cf. eq. B9 of Franx 1988)

$$\tan 2\psi = -\frac{T \sin 2\varphi \cos \vartheta}{\sin^2 \vartheta - T \left(\cos^2 \varphi - \sin^2 \varphi \cos^2 \vartheta \right)} \tag{3.1}$$

with $\sin 2\psi \sin 2\varphi \cos \vartheta \leq 0$ and $-\pi/2 \leq \psi \leq \pi/2$. A rotation over ψ transforms the coordinate system (x'', y'', z'') to (x', y', z'), with the x'-axis and y'-axis aligned with respectively the major and minor axis of Σ, whereas $z' = z''$ is along the line-of-sight.

The expressions in § 2.3 involve the velocity components in the confocal coordinate system (λ, μ, ν). The conversion to line-of-sight quantities can be done by four successive matrix transformations. First, we obtain the velocity components in the first octant of the intrinsic Cartesian coordinate system (x, y, z) by applying the matrix $\mathbf{Q}$, of which the first element is given by (cf. DL91)

$$Q_{11} = \mathrm{sign}(\lambda + \alpha) \sqrt{\frac{(\mu + \alpha)(\nu + \alpha)(\lambda + \beta)(\lambda + \gamma)}{(\alpha - \beta)(\alpha - \gamma)(\lambda - \mu)(\lambda - \nu)}}, \tag{3.2}$$

and the other elements follow horizontally by cyclic permutation of $\lambda \to \mu \to \nu \to \lambda$ and vertically by cyclic permutation of $\alpha \to \beta \to \gamma \to \alpha$. The second matrix uses the symmetries of the orbits to compute the appropriate signs of the intrinsic Cartesian velocities in the other octants. The result depends on whether or not the orbit has a definite sense of rotation in one of the confocal coordinates. For the three types of Abel components this results in the following matrices

$$
\begin{aligned}
\text{NR} \quad &: \quad \mathbf{S} = \mathrm{diag}[\mathrm{sgn}(x), \mathrm{sgn}(y), \mathrm{sgn}(z)] \\
\text{LR} \quad &: \quad \mathbf{S} = \mathrm{diag}[\mathrm{sgn}(xyz), \mathrm{sgn}(z), \mathrm{sgn}(y)] \\
\text{SR} \quad &: \quad \mathbf{S} = \mathrm{diag}[\mathrm{sgn}(y), \mathrm{sgn}(x), \mathrm{sgn}(xyz)]
\end{aligned}
\tag{3.3}
$$

Finally, the conversion from the intrinsic to the observer's Cartesian velocities involves the same projection and rotation as for the coordinates. We represent these two coordinate transformations respectively by the projection matrix

$$
\mathbf{P} = \begin{pmatrix} -\sin\varphi & \cos\varphi & 0 \\ -\cos\vartheta\cos\varphi & -\cos\vartheta\sin\varphi & \sin\vartheta \\ \sin\vartheta\cos\varphi & \sin\vartheta\sin\varphi & \cos\vartheta \end{pmatrix},
\tag{3.4}
$$

and the rotation matrix

$$
\mathbf{R} = \begin{pmatrix} \cos\psi & -\sin\psi & 0 \\ \sin\psi & \cos\psi & 0 \\ 0 & 0 & 1 \end{pmatrix}.
\tag{3.5}
$$

In this way, we arrive at the following relation

$$
\begin{pmatrix} v_{x'} \\ v_{y'} \\ v_{z'} \end{pmatrix} = \mathbf{M} \begin{pmatrix} v_\lambda \\ v_\mu \\ v_\nu \end{pmatrix}, \quad \text{with} \quad \mathbf{M} \equiv \mathbf{SPQR},
\tag{3.6}
$$

where the full transformation matrix $\mathbf{M}$ is thus a function of (λ, μ, ν), the constants (α, β, γ) and the viewing angles $(\vartheta, \varphi, \psi)$.

We can now write each velocity moment in the observer's Cartesian coordinate system (x', y', z') as a linear combination of the velocity moments in the confocal ellipsoidal coordinate system

$$
\mu_{ijk}(x', y', z') = \sum_{l,m,n} c_{l,m,n}\, \mu_{lmn}(\lambda, \mu, \nu),
\tag{3.7}
$$

with $i + j + k = l + m + n$. The coefficients $c_{l,m,n}$ are combinations of elements of $\mathbf{M}$, and can be obtained recursively as

$$
c_{l,m,n} = c_{l-1,m,n} + c_{l,m-1,n} + c_{l,m,n-1},
\tag{3.8}
$$

with the first order expressions given by

$$
c_{1,0,0} = M_{e_s 1}, \quad c_{0,1,0} = M_{e_s 2}, \quad c_{0,0,1} = M_{e_s 3},
\tag{3.9}
$$

and the index e_s is the sth element $(s = l + m + n)$ of the vector $\mathbf{e} = [1, .., 1, 2, .., 2, 3, .., 3]$. The number of integers 1 (#1) is equal to the value of the velocity moment index i, and similarly $\#2 = j$ and $\#3 = k$. For the density μ_{000} we have $c_{0,0,0} = 1$.

3.2   LINE-OF-SIGHT VELOCITY MOMENTS

Spectroscopic observations of the integrated light of galaxies provide the line-of-sight velocity distribution (LOSVD) as a function of position on the sky plane:

$$\mathcal{L}(x', y', v_{z'}) = \iiint f(E, I_2, I_3)\, \mathrm{d}v_{x'}\, \mathrm{d}v_{y'}\, \mathrm{d}z'. \tag{3.10}$$

The velocity moments of the LOSVD are

$$\mu_k(x', y') = \int_{-\infty}^{\infty} v_{z'}^k \mathcal{L}(x', y', v_{z'})\mathrm{d}v_{z'} \tag{3.11}$$

$$= \int_{-\infty}^{\infty} \mu_{00k}(x', y', z')\, \mathrm{d}z'. \tag{3.12}$$

The latter form follows upon substitution of the definition (3.10), rearranging the sequence of integration and using the definition of the intrinsic velocity moments of the DF. The lowest order velocity moments μ_0, μ_1 and μ_2 provide the surface mass density Σ, the mean line-of-sight velocity V and dispersion σ by

$$\Sigma = \mu_0, \quad V = \frac{\mu_1}{\mu_0}, \quad \text{and} \quad \sigma^2 = \frac{\mu_0\, \mu_2 - \mu_1^2}{\mu_0^2}, \tag{3.13}$$

as a function of (x', y').

The triple integral on the right-hand side of (3.10) can be evaluated relatively easily for the Abel DF (2.9), but is numerically cumbersome. On the other hand, the moments of the LOSVD follow by the single integration (3.12) and can be computed efficiently, even though the expressions for μ_{00k} are somewhat lengthy.

Whereas Σ, V and σ can be measured routinely, determinations of the higher order moments (μ_3, μ_4, ...), are in general more uncertain as they depend significantly on the wings of the LOSVD, which become quickly dominated by the noise in the observations. Instead of these true higher-order moments, one often uses the Gauss-Hermite moments (h_3, h_4, ...), which are much less sensitive to the wings of the LOSVD (van der Marel & Franx 1993; Gerhard 1993).

There is no simple (analytic) relation between the true moments (3.13) and the Gauss-Hermite moments, including the lower order moments Σ_{GH}, V_{GH} and σ_{GH} (but see eq. 18 of van der Marel & Franx 1993 for approximate relations to lowest order in h_3 and h_4). For this reason, we derive the Gauss-Hermite moments numerically. One way is to find the Gauss-Hermite LOSVD of which the numerically calculated true moments best-fit those from the Abel model. In Appendix C, we show however that this direct fitting of the true moments has various (numerical) problems, which can cause the resulting Gauss-Hermite moments to be significantly different from their true values. Instead, we (re)construct the LOSVD from the true moments by means of an Edgeworth expansion and then fit a Gauss-Hermite series to it. With this alternative method the Gauss-Hermite moments can be computed accurately and efficiently.

3.3   SURFACE BRIGHTNESS

The surface brightness follows upon integration of the luminosity density along the line-of-sight. The luminosity density in turn is related to the mass density $\rho_\star$ via the

stellar mass-to-light ratio $M_\star/L$. Whereas $\rho_\star$ is the zeroth-order velocity moment of the DF (eq. 2.8) that describes the distribution of the luminous matter, ρ_S is associated to the potential V_S and hence contains all matter, including possible dark matter. This means that in general the surface brightness cannot be obtained from ρ_S (or from V_S) and vice versa, without knowing (or assuming) the distribution of the dark matter. However, when the dark matter fraction is assumed to be constant, we only have to multiply ρ_S by a constant factor (<1) to obtain $\rho_\star$. This means that ρ_S is related to the luminosity density via a total mass-to-light ratio M/L which is $M_\star/L$ multiplied by the same factor. When in addition $M_\star/L$ does not change (e.g., due to variation in the underlying stellar populations), M/L is constant, i.e., mass follows light.

While in the outer parts of late-type galaxies the presence of dark matter, as predicted by the cold dark matter paradigm for galaxy formation (e.g., Kauffmann & van den Bosch 2002), was demonstrated convincingly already more than two decades ago (e.g., van Albada et al. 1985), the proof in the outer parts of early-type galaxies remains uncertain (e.g., Romanowsky et al. 2003), mainly due to a lack of kinematic constraints. As a consequence, in the outer parts of galaxies, commonly a simple functional form for the dark matter distribution is assumed, often the universal profile from the CDM paradigm (Navarro, Frenk & White 1997).

The dark matter distribution in the inner parts of galaxies is probably even more poorly understood (e.g., Primack 2004). Comparing the (total) M/L from dynamical modeling with the (stellar) $M_\star/L$ from color and absorption line-strength measurements can constrain the dark matter distribution (e.g., Cappellari et al. 2005). But due to uncertainties in the stellar population models, even the dark matter fraction is uncertain, let alone the shape of the dark matter distribution. The use of strong gravitational lensing to constrain the total mass distribution, in combination with dynamical modeling seems to be a promising way to study in detail the fraction and shape of the dark matter in the inner parts of galaxies (e.g., Treu & Koopmans 2004; see also Chapter 6 of this thesis). However, in current dynamical studies of the central parts of early-type galaxies, it is commonly assumed that mass follows light. As we saw above, after deprojection of the observed surface brightness for a given viewing direction, a simple scaling with the constant M/L then yields the total mass density ρ_S, from which the potential can be determined by solving Poisson's equation.

In the case of a constant mass-to-light ratio, we can also first multiply the surface brightness with this mass-to-light ratio and then deproject the resulting *surface* mass density to obtain the *intrinsic* mass density. The surface mass density that corresponds to the DF is Σ, defined in eq. (3.13). The surface mass density Σ_S related to the potential V_S has concentric isodensity contours that show no twist (e.g., Franx 1988).

3.4   COMBINATION OF MULTIPLE DF COMPONENTS

Until now, we have chosen the Abel DF to be a function of a single variable $S = -E + wI_2 + uI_3$, and we have separated it in three component types, non-rotating (NR), long-axis rotating (LR) and short-axis rotating (SR), but we have not made any assumption about the form of the DF (apart from the obvious requirement that it has to be non-negative everywhere and that it decreases to zero at large radii). Following MD99, we choose the DF to be a linear combination of basis functions of the form

$$f_\delta(S) = \left(\frac{S - S_{\min}}{1 - S_{\min}} \right)^\delta ,\qquad\qquad(3.14)$$

with δ a positive constant and $S_{\lim} \leq S_{\min} \leq S \leq 1$, and $S_{\lim}$ given in Fig. 2.

Once the potential V_S is known, we use the relations from § 2.3 together with the expressions in Appendix B, to compute the intrinsic velocity moments for the NR, SR and LR components in an efficient way, where at most the integral over S has to be evaluated numerically. For the NR components this integral can even be evaluated explicitly, resulting in

$$\mu_{lmn,\delta}^{\mathrm{NR}}(\lambda, \mu, \nu) = \sqrt{\frac{[2(S_{\max} - S_{\min})]^{l+m+n+3}}{H_{\mu\nu}^{l+1} H_{\nu\lambda}^{m+1} H_{\lambda\mu}^{n+1}}} \left(\frac{S_{\max} - S_{\min}}{1 - S_{\min}}\right)^{\delta} B(\tfrac{l+1}{2}, \tfrac{m+1}{2}, \tfrac{n+1}{2}, \delta+1), \quad (3.15)$$

where $S_{\max} = S_{\mathrm{top}}(\lambda, \mu, \nu)$ (cf. eq. 2.14). For a given viewing direction and mass-to-light ratio, we can then convert the intrinsic velocity moments to observable quantities as described in § 3.1–3.3. The observables depend on the choice of the DF parameters w, u and δ, they are different for each component type, and for the rotating components (LR and SR), they also depend on the sense of rotation around the axis of symmetry[4]. By combining the observables for a set of such DF components, we can construct realistic galaxy models. Since the mean line-of-sight velocity, velocity dispersion and higher order Gauss-Hermite velocity moments, are non-linear functions of the DF, we cannot directly combine these observables in a linear way.

Instead, we use the projected velocity moments (eq. 3.12) of the DF components, which we add together after multiplying each of them with a constant weight. We convert the resulting combined projected velocity moments to observables. Since the mass included in each DF component is different, we multiply the weights with the mass of the corresponding DF component, divided by the total (luminous) mass. In this way, we obtain the mass fractions per DF component.

4   TRIAXIAL THREE-INTEGRAL GALAXY MODELS

After choosing a Stäckel potential, we investigate the shape of the density generated by the Abel DF components, and use these components to construct a triaxial galaxy model with three integrals of motion.

4.1   ISOCHRONE POTENTIAL AND DENSITY

There are various choices for the potential and density that provide useful test models for comparison with the kinematics of triaxial elliptical galaxies (e.g., Arnold et al. 1994). One option is to consider the so-called perfect ellipsoid, for which Statler (1987) already computed numerical Schwarzschild models and Hunter & de Zeeuw (1992) investigated the maximum streaming thin orbit models. It has a density distribution stratified on similar concentric ellipsoids, but the potential function $U(\tau)$ contains elliptic integrals, which slows down numerical calculations. An alternative is to consider the set of models introduced by de Zeeuw & Pfenniger (1988), which have nearly ellipsoidal density figures, and have a potential and density that are evaluated easily and swiftly. They are defined by the choice:

$$U(\tau) = -GM(\sqrt{\tau} - \sqrt{-\alpha})(\sqrt{\tau} - \sqrt{-\gamma}) \left(\sqrt{\tau} + \frac{\sqrt{\alpha\gamma} - \beta}{\sqrt{-\alpha} + \sqrt{-\gamma}}\right), \quad (4.1)$$

---

[4]To change only the sense of rotation, the observables do not have to be recomputed, as a simple change in the sign of the odd velocity moments is sufficient.

so that the triaxial Stäckel potential has the elegant form

$$V_S(\lambda, \mu, \nu) = \frac{-GM\left(\sqrt{\lambda\mu} + \sqrt{\mu\nu} + \sqrt{\nu\lambda} - \beta\right)}{(\sqrt{\lambda} + \sqrt{\mu})(\sqrt{\mu} + \sqrt{\nu})(\sqrt{\nu} + \sqrt{\lambda})}, \tag{4.2}$$

where we set $GM = \sqrt{-\gamma} + \sqrt{-\alpha}$ to normalize V_S to -1 in the center. In the oblate axisymmetric limit this potential is that of the Kuzmin-Kutuzov (1962) models of De-jonghe & de Zeeuw (1988), and in the spherical limit it reduces to Hénon's (1959) isochrone. For all these models, V_S along the short z-axis is identical to the isochrone potential $-GM/(\sqrt{\tau} + \sqrt{-\alpha})$. We therefore refer to models with $U(\tau)$ of the form (4.1) as isochrone models. Since the potential falls of as $1/r$ at large radii, all these models have finite total mass.

The expressions for the integrals of motion are given in (2.5), where $U[\lambda, \mu, \nu] = V_S$ and the third order divided difference $U[\lambda, \mu, \nu, \sigma]$ is given by the symmetric expression

$$U[\lambda, \mu, \nu, \sigma] = -GM \frac{\sqrt{\lambda\mu\nu} + \sqrt{\mu\nu\sigma} + \sqrt{\nu\sigma\lambda} + \sqrt{\sigma\lambda\mu} - \beta(\sqrt{\lambda} + \sqrt{\mu} + \sqrt{\nu} + \sqrt{\sigma})}{(\sqrt{\lambda}+\sqrt{\mu})(\sqrt{\lambda}+\sqrt{\nu})(\sqrt{\lambda}+\sqrt{\sigma})(\sqrt{\mu}+\sqrt{\nu})(\sqrt{\mu}+\sqrt{\sigma})(\sqrt{\nu}+\sqrt{\sigma})}. \tag{4.3}$$

These isochrone models have the convenient property that the expressions for the potential and the integrals of motion contain only elementary functions of the (confocal ellipsoidal) coordinates and have no singularities.

The same is true for the associated mass density ρ_S, of which the expression is given in Appendix C of de Zeeuw & Pfenniger (1988), and a contour plot of ρ_S in the (x, z)-plane is shown in their Fig. 2. These authors also derive the axis ratios of ρ_S in the center (their eq. C7) and at large radii (their eq. C11), in terms of the axis ratios ζ and ξ of the confocal ellipsoidal coordinate system, defined as

$$\zeta^2 = \beta/\alpha, \quad \xi^2 = \gamma/\alpha. \tag{4.4}$$

Although ρ_S becomes slightly rounder at larger radii, its axis ratios remain smaller than unity (for $\xi < \zeta < 1$) because at large radii $\rho_S \sim 1/r^4$. Characteristic values for the axis ratios can be obtained from the (normalized) moments of inertia along the principal axes of the density,

$$a^2 = \frac{\int x^2 \rho(x, 0, 0)\, dx}{\int \rho(x, 0, 0)\, dx}, \tag{4.5}$$

where the intermediate and short semi-axis length, b and c, of the inertia ellipsoid follow from the long semi-axis length a by replacing x with y and z respectively. Taking for example $\zeta = 0.8$ and $\xi = 0.64$, the semi-axis lengths of the inertia ellipsoid result in the characteristic axis ratios $b_S/a_S = 0.89$ and $c_S/a_S = 0.82$ for the density ρ_S. The contours of the projected density are nearly elliptic with slowly varying axis ratios.

4.2   THE SHAPE OF THE LUMINOUS MASS DENSITY

Whereas the shape of the (total) mass density ρ_S is fixed by the choice of the potential V_S, and ζ and ξ (4.4), the shape of the (luminous) density $\rho_\star$, which is the zeroth order velocity moment of the DF (eq. 2.8), also depends on the DF parameters w, u and δ, and the type of component. For $\zeta = 0.8$ and $\xi = 0.64$, we show in Fig. 3 for non-rotating DF components the characteristic axis ratios of the corresponding density, as
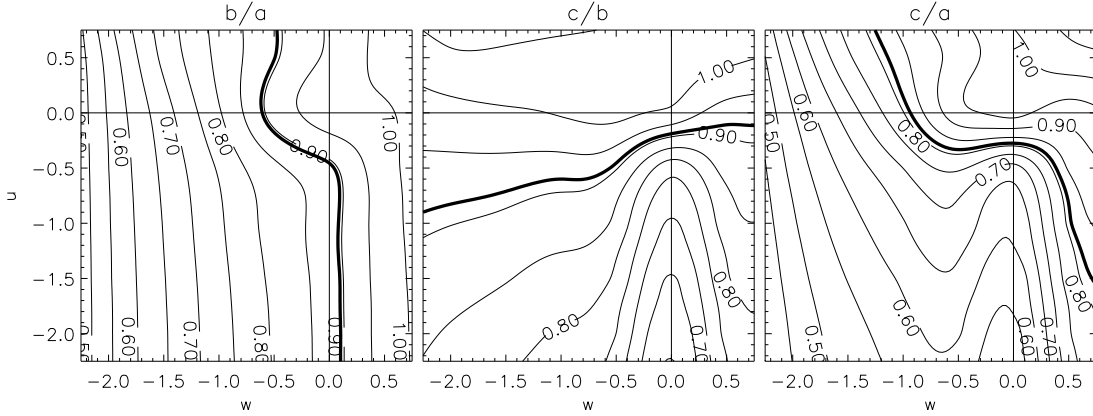
FIGURE 3 — *The characteristic axis ratios of the luminous mass density for a non-rotating Abel component, as function of the DF parameters w and u, and $\delta = 1$. The axis ratios of the confocal ellipsoidal coordinate system are $\zeta = 0.8$ and $\xi = 0.64$. The thick contours are drawn at the levels that correspond to the characteristic axis ratios of the total mass density ρ_S, associated with the underlying isochrone Stäckel potential (4.2). The intermediate-over-long axis ratio b/a depends mainly on w, the short-over-intermediate axis ratio c/b depends mainly on u, and c/a is the product of the previous two.*

function of w and u. We have set $\delta = 1$, but the axis ratios depend only weakly on it, with $\rho_\star$ becoming slightly flatter for increasing δ. The thick contours are drawn at the levels that correspond to the values of the characteristic axis ratios of ρ_S, respectively $a_S/b_S = 0.89$, $c_S/b_S = 0.91$ and $c_S/a_S = 0.82$. These values are independent of w and u (as well as the other DF parameters).

While the intermediate-over-long axis ratio b/a increases with increasing w, its value is nearly independent of u. By contrast, the short-over-intermediate axis ratio c/b, is nearly independent of w, and increases with increasing u. The short-over-long axis ratio c/a is the product of the previous two axis ratios and thus depends on both w and u. When both w and u are negative, the density $\rho_\star$ has its long-axis along the x-axis and its short-axis along the z-axis, in the same way as the potential V_S and the associated density ρ_S. Above certain positive values of either w or u, the axis ratios become larger than unity, which means that $\rho_\star$ is no longer aligned with the underlying coordinate system in the same way as V_S and ρ_S. For example, when $w = -0.5$ and $u = 0.5$, $b/a < 1$ but $c/b > 1$, so that in this case $\rho_\star$ has its short axis along the y-axis.

A change in the sign of w and u has a strong effect on the radial slope of $\rho_\star$. In Fig. 4, the radial profiles of $\rho_\star$ along the principal axes are shown for four combinations of w and u. The density is normalized to the central value ρ_0. To set the dimension of the radius r, we have set the scale length l_α, defined as

$$l_\alpha = \sqrt{-\alpha}, \tag{4.6}$$

to $10''$. For given axis ratios ζ and ξ of the confocal ellipsoidal coordinate system, we calculate all quantities with respect to unit scale length. At the end we scale the resulting Abel model, depending on the value of l_α (in arcsec) and the assumed distance D (in Mpc). The profiles along the y-axis (dotted curves) and along the z-axis (dashed curves) are arbitrarily offset vertically with respect to the profile along the
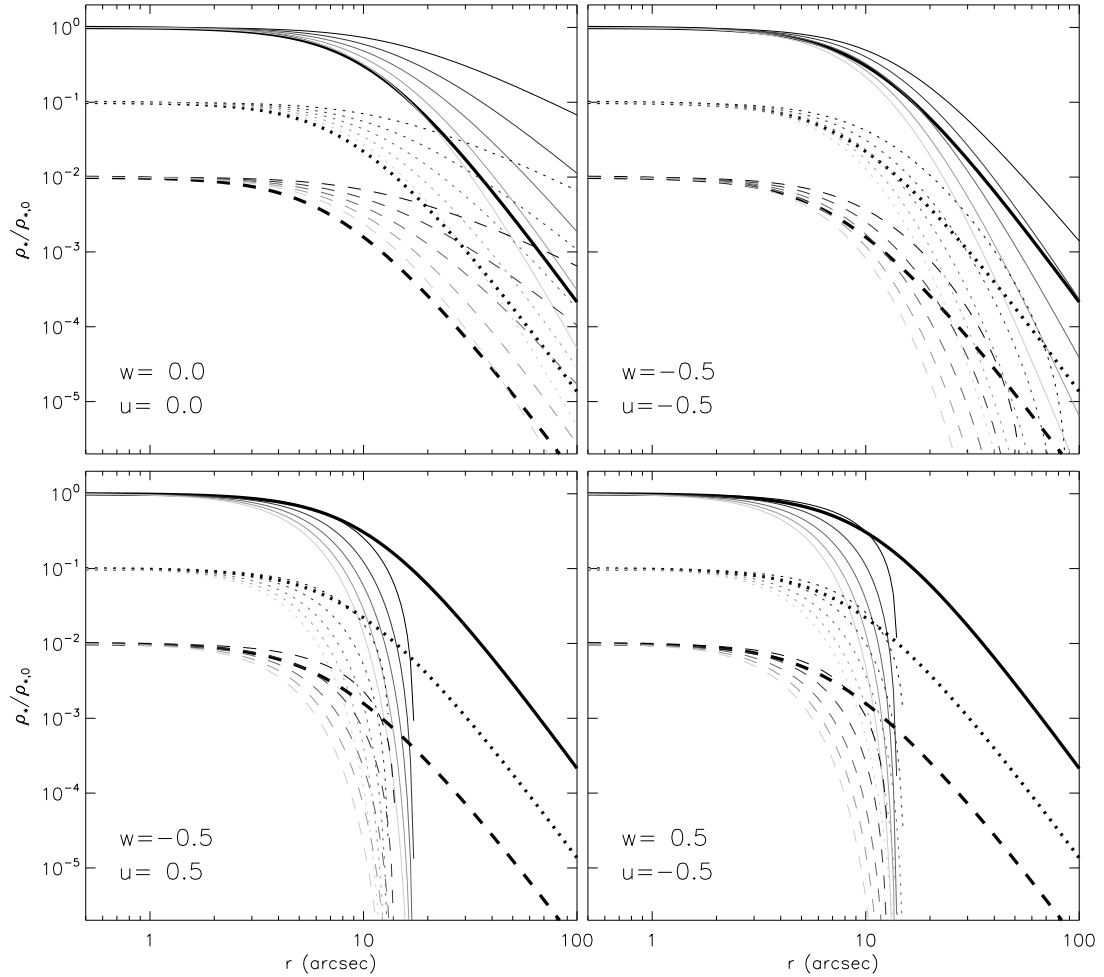
FIGURE 4 — *Principal axes profiles of the luminous mass density $\rho_\star$ for a non-rotating Abel component, normalized to the central value $\rho_{\star,0}$. Each panel is for a different combination of the DF parameters w and u, while the grey scale indicates variation in δ from zero (darkest curve) to four (lightest curve), in unity steps. The profiles along the y-axis (dotted curves) and along the z-axis (dashed curves) are arbitrarily offset vertically with respect to the profile along the x-axis (solid curves) to enhance the visualization. The thick black curves show the profiles for the (total) mass density ρ_S, associated with the underlying isochrone Stäckel potential (4.2), with $\zeta = 0.8$ and $\xi = 0.64$, and scale length $a = 10''$. When the value of either w or u is positive (bottom panels), the profiles show a break at around the scale-length, so that these compact components may be used to represent kinematically decoupled components.*

x-axis (solid curves) to enhance the visualization. The thin curves are the profiles of the (luminous) mass density $\rho_\star$ for varying δ, from $\delta = 0$ (darkest curve) to $\delta = 4$ (lightest curve), in unit steps. The thick black curves show the profiles for the (total) mass density ρ_S, which is independent of w, u and δ.

The profiles of $\rho_\star$ become steeper for increasing δ and for increasing absolute values of w and u. In particular, when either w or u becomes positive (bottom panels), the

profiles suddenly become much steeper and drop to zero already at relatively small radii. The resulting Abel components are thus compact and, as we saw above, can be different in shape and orientation from the main body of the galaxy model. Therefore, they can be used to represent kinematically decoupled components. When both $w \leq 0$ and $u \leq 0$ (top panels), $\rho_\star$ falls off much more gently and the Abel components cover a larger region. When $w = u = 0$ (top left panel), so that the DF only depends on energy, the profiles as well as the shape (Fig. 3) of $\rho_\star$ can even be flatter than those of ρ_S. However, already for small non-zero values of w and u, generally $\rho_\star \leq \rho_S$ everywhere in the galaxy model, and $\rho_\star < \rho_S$ in the outer parts. Although self-consistency $\rho_\star = \rho_S$ is only possible in the spherical case (for fixed values of w and u, see § 2.3), we can choose the parameters w, u and δ so that $\rho_\star \sim \rho_S$. At the same time, having $\rho_\star < \rho_S$ in the outer parts of the galaxy model, allows us to take into account a dark halo contribution.

The shape of $\rho_\star$ can furthermore change due to the additional contribution from long-axis rotating and short-axis rotating components. Although these components have no density along respectively the long-axis and short-axis, the behavior of their overall shape as function of w, u and δ is similar as above for the corresponding non-rotating components.

The above analysis shows that, given the triaxial isochrone potential (4.2), we can use Abel components to construct a galaxy model with a realistic density. Depending on the choice of w, u and δ, the galaxy model can contain compact (kinematically decoupled) components and account for possible dark matter (in the outer parts). Furthermore, we show below that even with a small number DF components, enough kinematic variation is possible to mimic the two-dimensional kinematic maps of early-type galaxies provided by observations with integral-field spectrographs such as SAURON. This means that we can construct simple but realistic galaxy models to test our Schwarzschild software (§ 6 and 7).

4.3   A triaxial Abel model

As before, we choose the isochrone Stäckel potential (4.2), we take $\zeta = 0.8$ and $\xi = 0.64$ for the axis ratios of the coordinate system (4.4), resulting in a triaxiality parameter (2.6) of about $T = 0.61$, and we set the scale length (4.6) to $l_\alpha = 10''$. Assuming a distance of $D = 20$ Mpc and a total mass of 10^{11} M$_\odot$ results in a central value for the potential $V_0 \sim 2.5 \times 10^6$ km^2 s^{-2}, which also sets the unit of velocity. We restrict the number of DF components to three, one of each type. For the first component of type NR we set $w = -0.5$, $u = -0.5$ and $\delta = 1$, so that the shape of the corresponding density is similar to that of ρ_S, except in the outer parts where a steeper profile mimics the presence of dark matter (see Figs. 3 and 4). For the second and third component, respectively of type LR and SR, we adopt the same parameters, expect that we take $u = 0.5$ for the SR component, which therefore is more compact than the NR and LR component.

For each DF component, we calculate the intrinsic true velocity moments up to fifth ($s = 5$) order and integrate them along the line-of-sight, which we set by choosing $\vartheta = 70°$ and $\varphi = 30°$ for the viewing angles. After rotation over the misalignment angle $\psi = 101°$ (3.1), we obtain the projected true velocity moments μ_k ($k = 0, \dots, 5$) shown in Fig. 5. The parameters of each DF component are given on the right. The grey scale indicates the range of the true velocity moment in each panel, from minimum (black) to maximum value (white). The NR component has zero odd velocity moments. For the LR and SR component, the even velocity moments show a decrease in the center,
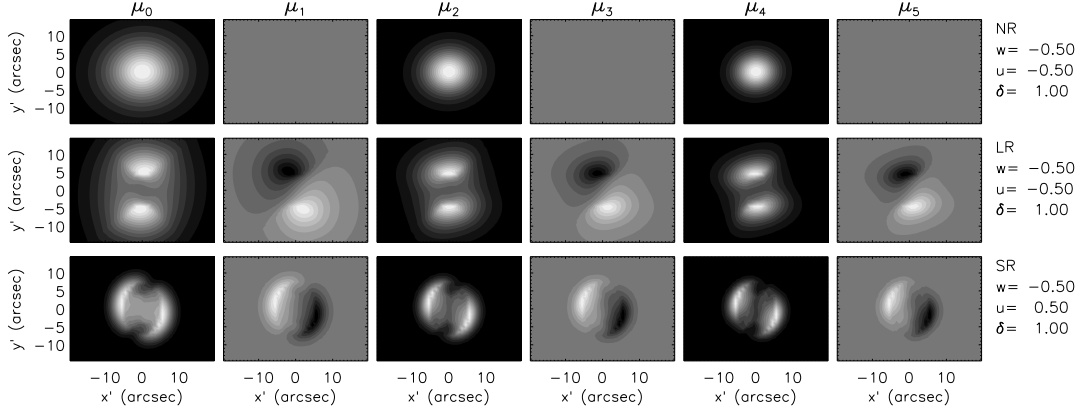
FIGURE 5 — *From left to right: Projected true moments μ_k (k = 0, ..., 5) of Abel DF components for a model with the triaxial separable isochrone potential (4.2) with $\zeta = 0.8$ and $\xi = 0.64$ (T = 0.61), and scale length $a = 10''$. The model is placed at a distance of D = 20 Mpc and the adopted viewing angles are $\vartheta = 70°$ and $\varphi = 30°$. From top to bottom: A non-rotating (NR), long-axis rotating (LR) and short-axis rotating (SR) Abel component, with the corresponding DF parameters w, u and δ given on the right.*

because these components have zero density along respectively the intrinsic long and short axis. We add the true velocity moments of the NR, LR and SR components, weighted with mass fractions of respectively 80%, 10% and 10%. From the resulting combined true velocity moments, we construct the Edgeworth LOSVD and fit a Gauss-Hermite series (see Appendix C), to obtain maps of the mean line-of-sight surface mass density Σ, velocity V, velocity dispersion σ and higher-order moments h_3 and h_4. We convert Σ to the surface brightness by dividing by a constant stellar mass-to-light ratio of $M_\star/L = 4 \, \mathrm{M_\odot/L_\odot}$.

To convert these 'perfect' kinematics to 'realistic' observations, similar to those obtained with SAURON (Bacon et al. 2001), we finally apply the following steps. Each of the maps consist of 30 by 40 square pixels of $1''$ in size. Using the adaptive spatial 2D-binning scheme of Cappellari & Copin (2003), we bin the pixels according to the criterion that each of the resulting (Voronoi) bins contains a minimum in signal-to-noise (S/N), which we take proportional to the square root of the surface brightness. For the mean errors in the kinematics we adopt the typical values of $10 \, \mathrm{km \, s^{-1}}$ for V and σ and 0.03 for h_3 and h_4 in the kinematics of a representative sample of early-type galaxies observed with SAURON (Emsellem et al. 2004). We then weigh these values with the S/N in each bin to mimic the observed variation in measurement errors across the field. Finally, we use the computed measurement errors to (Gaussian) randomize the kinematic maps. In this way, we include the randomness that is always present in real observations. The resulting kinematic maps are shown in the top panels of Fig. 6. Because of the eight-fold symmetry of the triaxial model, the maps are always point-symmetric, apart from the noise added.

4.4   REALISTIC GALAXY MODELS WITH MULTIPLE DF COMPONENTS

In the above triaxial Abel model we only use three DF components to obtain a transparent (test) galaxy model, but with rich enough internal dynamics to provide observ-
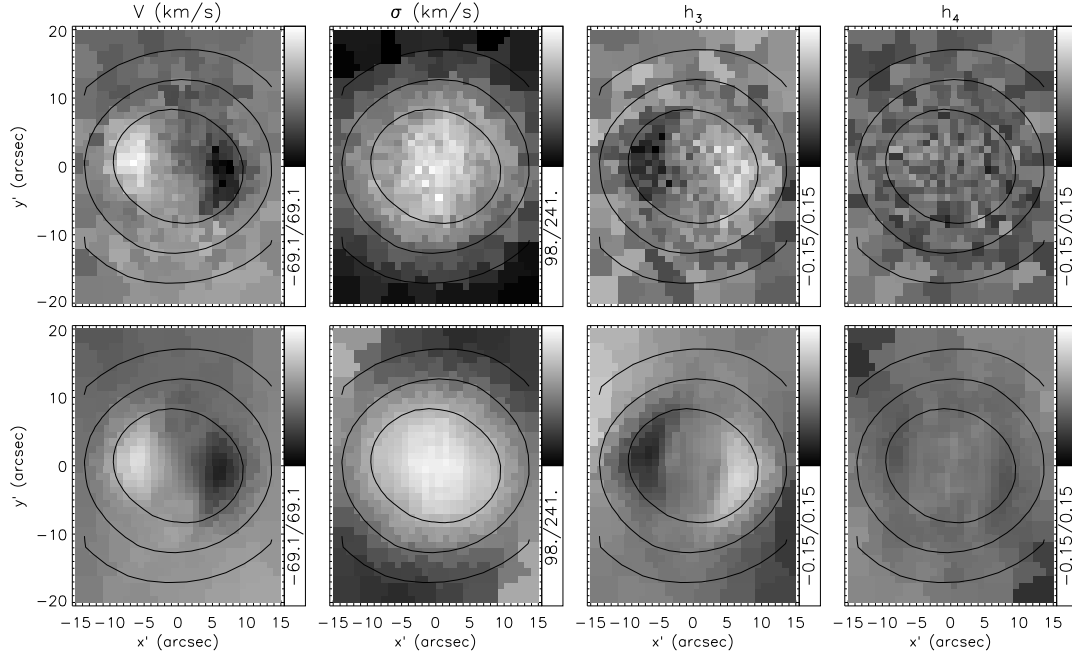
FIGURE 6 — *Kinematic maps for a triaxial Abel model (top; see § 4.3) and for the best-fit triaxial Schwarzschild model (bottom; see § 6). From left to right: mean line-of-sight velocity V (in km s^{-1}), velocity dispersion σ (in km s^{-1}) and Gauss-Hermite moments h_3 and h_4. The line-of-sight kinematics of the input Abel model have been converted to observables with realistic measurement errors as described in the text. Isophotes of the surface brightness of the Abel model are overplotted in each map. At the right side of each map, the (linear) scale of the corresponding kinematics is indicated by the grey scale bar, and the limits are given below. (See p. 253 for a color version of this figure.)*

ables that mimic the kinematics of real early-type galaxies. More general Abel models can be obtained by a (linear) combination of more DF components, with varying functional forms of the variable S and different values of the parameters w and u. We saw in § 4.2 that by changing w and u the DF components can have a large range in different shapes, and the same is true for the corresponding intrinsic velocity moments (see also Fig. 9–11 of DL91).

By summing a series of DF components over w and u [with possibly different functional dependences of $f(S)$], one might expect to cover a large fraction of all physical DFs. Due to the different values of w and u, such a sum of DF components is no longer a function of the same, single variable S, so that the ellipsoidal hypothesis does not apply. Consequently, it becomes possible to construct (nearly) self-consistent dynamical models, with the (combined) luminous mass density $\rho_\star$ equal (or close) to the mass density ρ_S associated to the potential.

This combination of DF components provides an elegant way to (numerically) build three-integral galaxy models. Nuyten (2005, MSc thesis) used thirty DF components to fit the kinematic maps of the decoupled core galaxy NGC 4365 provided by observations with the integral-field spectrograph SAURON (Davies et al. 2001). The best-fit is reasonable, but deviates especially in the center due to the presence of a massive

black hole. We find constraints on the viewing direction and mass-to-light ratio, as well as a first estimate of the masses and a description of the intrinsic dynamical structure of the different orbital components, consistent with an independent determination by Statler et al. (2004). This preliminary investigation shows that Abel models with a few DF components, as in § 4.3, already provide quite a good representation of real early-type galaxies (see also MD96 for a similar application to Centaurus A).

5 AXISYMMETRIC THREE-INTEGRAL GALAXY MODELS

We now consider three-integral galaxy models in the axisymmetric limit. Various groups have successfully developed independent axisymmetric implementations of Schwarzschild's method and verified their codes in a number of ways. The published tests to recover a known (analytical) input model have been limited to spherical geometry or to an axisymmetric DF that is a function of the two integrals of motion E and L_z only. Here we present the velocity moments of the three-integral Abel DF in the axisymmetric limit and we choose again the isochrone form (4.1) for the potential. The properties of the resulting three-integral Kuzmin-Kutuzov models can be expressed explicitly in cylindrical coordinates. In § 7, we fit Schwarzschild models to the resulting observables to test our axisymmetric implementation of Schwarzschild's method.

5.1 VELOCITY MOMENTS OF AXISYMMETRIC ABEL MODELS

When two of the three constants α, β or γ are equal, the confocal ellipsoidal coordinates (λ, μ, ν) reduce to spheroidal coordinates and the triaxial Stäckel potential (2.3) becomes axisymmetric.

When $\beta = \alpha \neq \gamma$, we cannot use μ as a coordinate and replace it by the azimuthal angle ϕ, defined as $\tan \phi = y/x$. The relation between (λ, ϕ, ν) and the usual cylindrical coordinates (R, ϕ, z) is given by

$$R^2 = \frac{(\lambda + \alpha)(\nu + \alpha)}{\alpha - \gamma}, \quad z^2 = \frac{(\lambda + \gamma)(\nu + \gamma)}{\gamma - \alpha}. \tag{5.1}$$

The Stäckel potential $V_S(\lambda, \nu) = U[\lambda, -\alpha, \nu]$ is *oblate axisymmetric*. The corresponding integrals of motion follow by substitution of $\mu = -\beta = -\alpha$ in the expressions (2.5). The second integral of motion reduces to $I_2 = \frac{1}{2} L_z^2$ and the triaxiality parameter $T = 0$.

With the choice (2.9) for the DF, the expression for the velocity moments becomes

$$\mu_{lmn}(\lambda, \nu) = \sqrt{\frac{2^{l+m+n+3}}{H_{(-\alpha)\nu}^{l+1} H_{\nu\lambda}^{m+1} H_{\lambda(-\alpha)}^{n+1}}} \int_{S_{\min}}^{S_{\max}} T_{lmn} \left[S_{\text{top}}(\lambda, -\alpha, \nu) - S \right]^{(l+m+n+1)/2} f(S) \, dS, \tag{5.2}$$

where $H_{\sigma\tau}$ is defined in eq. (2.11) and $S_{\min} \geq S_{\lim}$, which follows from Fig. 2 for $\beta = \alpha$. The lower limit on w vanishes, so that it can have any value.

For the NR type of components $S_{\max} = S_{\text{top}}(\lambda, -\alpha, \nu)$, defined in eq. (2.14), and the expression for T_{lmn}^{NR} is as in eq. (2.15). The NR velocity moments $\mu_{lmb}^{\text{NR}}(\lambda, \nu)$ vanish when either l, m or n is odd. Since the only family of orbits that exists are the short-axis tube orbits, we can introduce net rotation (around the z-axis) by setting the DF to zero for $L_z < 0$, so that $\mu_{lmn}^{\text{SR}}(\lambda, \nu) = \frac{1}{2} \mu_{lmn}^{\text{NR}}(\lambda, \nu)$. These SR velocity moments vanish when either l or n is odd, but are non-zero if m is odd. They should be multiplied with $(-1)^m$ for net rotation in the opposite direction.

In the conversion to observables described in § 3, the matrix $\mathbf{Q}$, which transforms the velocity components $(v_\lambda, v_\phi, v_\nu)$ to (v_x, v_y, v_z), reduces to

$$\mathbf{Q} = \begin{pmatrix} A\cos\phi & -\sin\phi & -B\cos\phi \\ A\sin\phi & \cos\phi & -B\sin\phi \\ B & 0 & A \end{pmatrix}, \tag{5.3}$$

where A and B are defined as

$$A^2 = \frac{(\lambda+\gamma)(\nu+\alpha)}{(\lambda-\nu)(\alpha-\gamma)}, \quad B^2 = \frac{(\lambda+\alpha)(\nu+\gamma)}{(\lambda-\nu)(\gamma-\alpha)}. \tag{5.4}$$

Because of the symmetry around the short-axis, the azimuthal viewing angle φ looses its meaning and the misalignment angle $\psi = 0°$. We are left with only the polar viewing angle ϑ, which is commonly referred to as the inclination i. As a consequence, the projection matrix $\mathbf{P}$ is a function of i only and follows by substituting $\vartheta = i$ and $\varphi = 0$ in eq. (3.4), while the rotation matrix $\mathbf{R}$ in eq. (3.5) reduces to the identity matrix.

When $\beta = \gamma \neq \alpha$, we replace the coordinate ν by the angle χ, defined as $\tan\chi = z/y$. The resulting coordinates (λ, μ, χ) follow from the above coordinates (λ, ϕ, ν) by taking $\nu \to \mu$, $\phi \to \chi$, and $\gamma \to \alpha \to \beta$. The Stäckel potential $V_S(\lambda, \mu) = U[\lambda, \mu, -\gamma]$ is now *prolate axisymmetric*, and for the integrals of motion we set $\nu = -\beta = -\gamma$ in the expressions (2.5), so that $I_3 = \frac{1}{2}L_x^2$ and $T = 1$. The intrinsic velocity moments $\mu_{lmn}(\lambda, \mu)$ follow from eq. (5.2) by interchanging $\nu \leftrightarrow \mu$, $\gamma \leftrightarrow \alpha$ and $m \leftrightarrow n$. Taking $\beta = \gamma$ in Fig. 2, we see that now the upper limit on u vanishes. In this case, $S_{\max} = S_{\text{top}}(\lambda, \mu, -\gamma)$ for the NR components, and since we only have the long-axis tube orbits, we can introduce net rotation (around the x-axis) by setting the DF to zero for $L_x < 0$, so that $\mu_{lmn}^{\text{LR}}(\lambda, \mu) = \frac{1}{2}\mu_{lmn}^{\text{NR}}(\lambda, \mu)$. The LR velocity moments vanish if either l or m is odd and multiplication with $(-1)^n$ yields net rotation in the opposite direction. The matrix $\mathbf{Q}$, which transforms $(v_\lambda, v_\mu, v_\chi)$ to (v_x, v_y, v_z), in this case reduces to

$$\mathbf{Q} = \begin{pmatrix} C & -D & 0 \\ D\cos\chi & C\cos\chi & -\sin\chi \\ D\sin\chi & C\sin\chi & \cos\chi \end{pmatrix}, \tag{5.5}$$

where C and D follow from respectively A and B in (5.4) by replacing ν by μ. We substitute $\vartheta = \pi/2 - i$ and $\varphi = 0$ in eq. (3.4) to obtain the projection matrix $\mathbf{P}$. The rotation matrix $\mathbf{R}$ again reduces to the identity matrix.

5.2   KUZMIN-KUTUZOV POTENTIAL AND DENSITY

In the axisymmetric limit, the form (4.1) for $U(\tau)$ results in the Kuzmin-Kutuzov (1962) potential. We give the properties relevant for our analysis, while further details can be found in Dejonghe & de Zeeuw (1988), including expressions and plots of the mass density ρ_S, its axis ratios, and the two-integral DF $f(E, L_z^2)$ consistent with ρ_S [see also Batsleer & Dejonghe (1993), who also corrected a typographical error in $f(E, L_z^2)$].

When $\beta = \alpha$, the oblate axisymmetric potential $V_S(\lambda, \nu) = U[\lambda, -\alpha, \nu]$ and the third order divided difference $U[\lambda, -\alpha, \nu, \sigma]$, which both appear in the expressions for the integral of motions (2.5), have the simple forms

$$V_S(\lambda, \nu) = \frac{-GM}{\sqrt{\lambda} + \sqrt{\nu}}, \tag{5.6}$$

$$U[\lambda, -\alpha, \nu, \sigma] = \frac{-GM}{(\sqrt{\lambda} + \sqrt{\nu})(\sqrt{\lambda} + \sqrt{\sigma})(\sqrt{\nu} + \sqrt{\sigma})}, \tag{5.7}$$
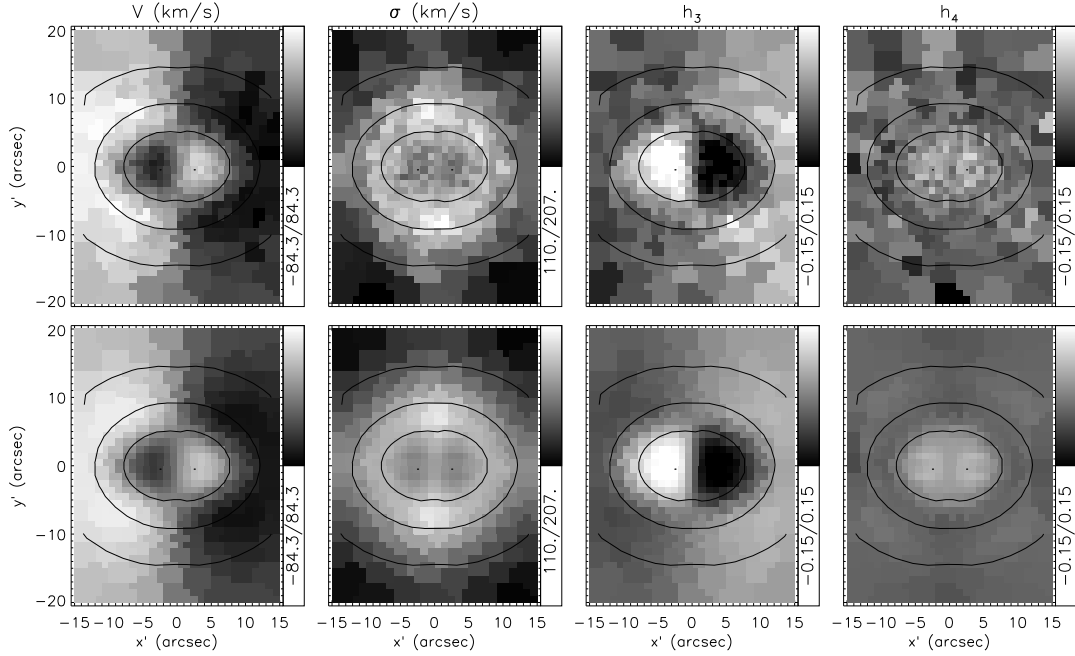
FIGURE 7 — *Kinematic maps for an oblate axisymmetric Abel model (top; see § 5.3) and for the fitted axisymmetric Schwarzschild model (bottom; see § 7). Parameters and grey scale are as in Fig. 6. (See p. 255 for a color version of this figure.)*

where again $GM = \sqrt{-\gamma} + \sqrt{-\alpha}$, so that $V_S = -1$ in the center. By means of the relations

$$\lambda + \nu = R^2 + z^2 - \alpha - \gamma, \quad \lambda\nu = \alpha\gamma - \gamma R^2 - \alpha z^2, \tag{5.8}$$

and $(\sqrt{\lambda} + \sqrt{\nu})^2 = \lambda + \nu + 2\sqrt{\lambda\nu}$ and $(\sqrt{\lambda} + \sqrt{\sigma})(\sqrt{\nu} + \sqrt{\sigma}) = \sqrt{\lambda\nu} + \sqrt{\sigma}(\sqrt{\lambda} + \sqrt{\nu}) + \sigma$, we can write the potential and integrals of motion explicitly as elementary expressions in the usual cylindrical coordinates.

When $\beta = \gamma$, the prolate potential $V_S(\lambda, \mu) = U[\lambda, \mu, -\gamma]$ and the third order divided difference $U[\lambda, \mu, -\gamma, \sigma]$ follow respectively from (5.6) and (5.7) by replacing ν by μ.

5.3 AN AXISYMMETRIC ABEL MODEL

The above constructed triaxial Abel model (§ 4.3) transforms into an oblate axisymmetric Abel model if we let ζ approach unity, while keeping $\xi = 0.64$ fixed. We keep the NR component with the same parameters, $u = w = -0.5$ and $\delta = 1$, but we exclude the LR component since long-axis tube orbits do not exist in an oblate axisymmetric galaxy. We include two SR components, one with the same parameters as the NR component, and for the other we set $u = 0.5$ and choose the sense of rotation in the opposite direction. The latter implies a compact counter-rotating component, which is clearly visible in the kinematic maps shown in the top panels of Fig. 7. The inclination is the same value as the polar angle ϑ for the triaxial Abel model, i.e. $i = 70°$, and the mass fractions of the three DF components are respectively 20%, 60% and 20%. Due to axisymmetry all maps are bi-symmetric and the velocity field shows a straight zero-velocity curve. The signatures of the counter-rotation are similar in the velocity

field and h_3 (but anti-correlated), and result in a decrease of σ and an increase of h_4 in the center.

6   RECOVERY OF TRIAXIAL GALAXY MODELS

We briefly describe our numerical implementation of Schwarzschild's method in tri-axial geometry (see van den Bosch et al. 2006 for a full description), which we then use to fit the observables of the triaxial Abel model constructed in § 4.3. We investigate the recovery of the intrinsic velocity moments and, through the distribution of the orbital mass weights, the recovery of the three-integral DF. We also determine the constraints placed on the viewing direction and the mass-to-light ratio.

6.1   TRIAXIAL SCHWARZSCHILD MODELS

The first step is to infer the gravitational potential from the observed surface bright-ness. This is done by means of the Multi-Gaussian Expansion method (MGE; e.g., Cappellari 2002), which allows for possible position angle twists and ellipticity varia-tions in the surface brightness. For a given set of viewing angles $(\vartheta, \varphi, \psi)$ (see § 3.1), the surface brightness is deprojected and multiplied by a mass-to-light ratio M/L to yield the intrinsic mass density, from which the gravitational potential then follows by solving Poisson's equation. Orbits are calculated numerically in the resulting grav-itational potential. To obtain a representative library of orbits, the integrals of motion have to be sampled well. The energy can be sampled directly, but since the other integrals of motion are generally not known, we start, at a given energy, orbits from a polar grid in the (x, z)-plane, which is crossed perpendicularly by all families of (reg-ular) orbits. To have enough box orbits to support the triaxial shape, we also start orbits by dropping them from the equipotential surface (Schwarzschild 1979, 1993).

Assigning a mass weight γ_j to each orbit j from the library, we compute their combined properties and find the weighted superposition that best fits the observed surface brightness and (two-dimensional) kinematics. However, the resulting orbital weight distribution may vary rapidly, and hence probably corresponds to an unreal-istic DF. To obtain a smoothly varying DF, we both dither the orbits by considering a bundle of integrated orbits that were started close to each other, and we regularize when looking for the best-fit set of orbital weights by requiring them to vary smoothly between neighboring orbits (in integral space). The best-fit Schwarzschild model fol-lows from the minimum in

$$\chi^2 = \sum_{i=1}^{N_O} \left(\frac{O_i - O_i^\star}{\Delta O_i} \right)^2 , \tag{6.1}$$

where N_O is the number of (photometric and kinematic) observables O_i with associ-ated error ΔO_i and $O_i^\star$ is the corresponding model prediction.

In this case, we can use directly the isochrone Stäckel potential V_S of the triaxial Abel model. However, to closely simulate the Schwarzschild modeling of real galaxies, we infer the potential from a deprojection of an MGE fit of the surface mass density Σ_S generated by V_S. The resulting potential reproduces V_S to high precision.

We compute a library of orbits by sampling 21 energies E via a logarithmic grid in radius from $1''$ to $224''$ that contains ≥ 99.9 per cent of the total mass. At each energy, we construct a uniform polar grid of 7 radii by 8 angles within the region in the first quadrant of the (x, z)-plane that is enclosed by the equipotential and the thin orbit
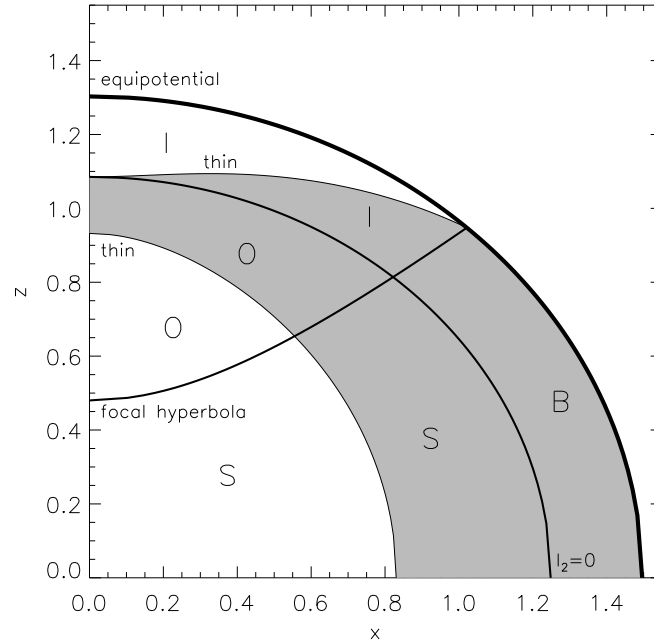
FIGURE 8 — *The (x, z)-plane for a triaxial isochrone potential (4.2) with $\zeta = 0.8$ and $\xi = 0.64$, at a given energy E (cf. Schwarzschild 1993). The region inside the equipotential (solid curve) is crossed perpendicularly by the four general orbit families: box (B) orbits, inner (I) and outer (O) long-axis tube orbits and short-axis (S) tube orbits. They are separated by the focal hyperbola of the ellipsoidal coordinate system in which the equations of motion separate, and the curve on which the second integral of motion I_2 is zero. The thin orbits with maximum streaming divide the regions of the tube orbits in two parts, each of which is crossed once by each tube orbit. By considering only the grey region, we sample all orbits without duplication.*

curves (Fig. 8). In addition, we drop box orbits from a similar uniform polar grid on the equipotential surface in the first octant. This results in a total of $21 \times 7 \times 8 \times 2 = 2352$ starting positions, from each of which a bundle of 6^3 orbits are started. Taking into account the two senses of rotation of the tube orbits, this results in a total 762048 orbits that are numerically integrated in the potential.

The velocities of each bundle of orbits are summed in histograms with 201 bins, at a velocity resolution of 10 km s^{-1}. The weighted sum of the velocity histograms is fitted to the intrinsic density $\rho_\star$ and simultaneously their projected values are fitted to the observed surface brightness and higher-order velocity moments. At the same time, the orbital weights are regularized in E and in the starting positions by minimizing their second order derivatives and requiring that these derivatives are smaller than the smoothening parameter (e.g., Cretton et al. 1999), which we set to $\Delta = 4$.

6.2   INTRINSIC MOMENTS

We calculate the intrinsic first and second order velocity moments of the Schwarzschild model by combining the appropriate moments of the orbits that receive weight in the superposition, and investigate how well they compare with the intrinsic veloc-
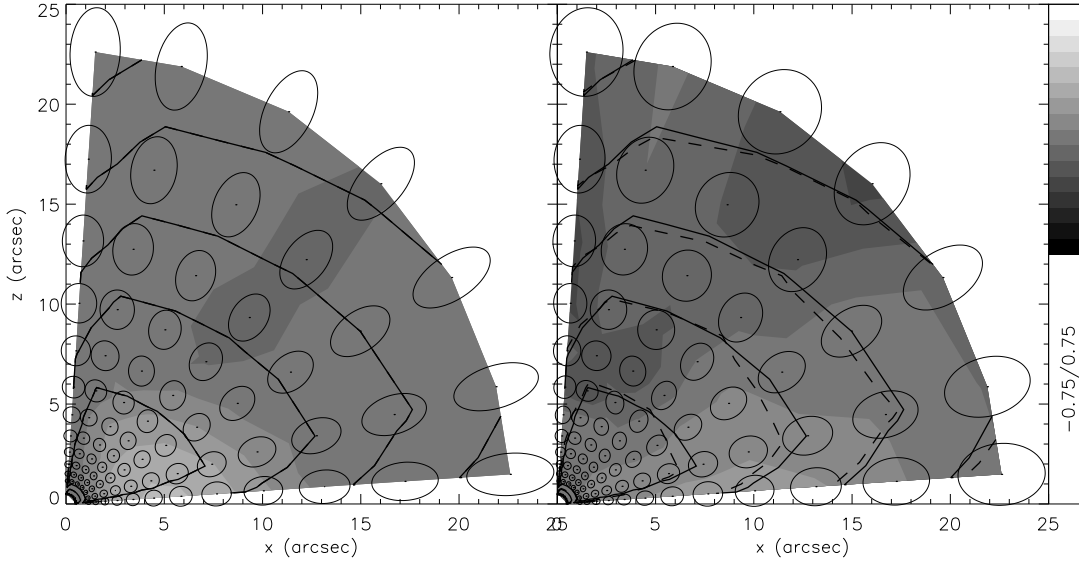
FIGURE 9 — *The grey scale represents the mean motion $\langle v_y \rangle$ perpendicular to the (x, z)-plane, normalized by σ_{RMS} (excluding the axes to avoid numerical problems), for a triaxial Abel model (left) and for the best-fit triaxial Schwarzschild model (right). The ellipses are cross sections of the velocity ellipsoid with the (x, z)-plane. The black curves are contours of constant mass density in steps of one magnitude, for the input Abel model (solid) and for the fitted Schwarzschild model (dashed). See § 6.2 for details. (See p. 254 for a color version of this figure.)*

ity moments of the Abel model. In general, there are three first $\langle v_t \rangle$ and six second order velocity moments $\langle v_s v_t \rangle$ ($s, t = x, y, z$). Combining them yields the six dispersion components σ_{st} of the velocity ellipsoid, where $\sigma_{st}^2 \equiv \langle v_s v_t \rangle - \langle v_s \rangle \langle v_t \rangle$.

To facilitate visualization, we restrict the analysis to a single plane. We choose the (x, z)-plane, as it is crossed perpendicularly by all four (major) orbit families. Because $\langle v_x \rangle = \langle v_z \rangle = \sigma_{xy} = \sigma_{yz} = 0$, we are left with $\langle v_y \rangle$ perpendicular to the (x, z)-plane as the only non-vanishing mean motion and σ_{zx} in the (x, z)-plane as the only non-vanishing cross-term. The average root-mean-square velocity dispersion σ_{RMS} is given by $\sigma_{RMS}^2 = (\sigma_x^2 + \sigma_y^2 + \sigma_z^2)/3$, where $\sigma_x \equiv \sigma_{xx}$, $\sigma_y \equiv \sigma_{yy}$ and $\sigma_z \equiv \sigma_{zz}$.

The ratio $\langle v_y \rangle / \sigma_{RMS}$ of ordered over random motion is a measure of the importance of rotation for the gravitational support of a galaxy. In Fig. 9, the grey scale shows the values of this ratio in the (x, z)-plane, for the triaxial Abel model (left panel) and for the fitted triaxial Schwarzschild model (right panel). The ellipses show the cross sections of the velocity ellipsoid with the (x, z)-plane. In a Stäckel potential the axes of the velocity ellipsoid are aligned with the confocal ellipsoidal coordinate system (e.g., Eddington 1915; van de Ven et al. 2003). As a result, one of the axes of the velocity ellipsoid is perpendicular to the (x, z)-plane, with semi-axis length σ_y. The other two axes lie in the (x, z)-plane and have semi-axis lengths given by

$$\sigma_\pm^2 = \tfrac{1}{2}(\sigma_x^2 + \sigma_y^2) \pm \sqrt{\tfrac{1}{4}(\sigma_x^2 - \sigma_y^2)^2 + \sigma_{xy}^4}. \tag{6.2}$$

The ellipses are radially elongated, corresponding to a radial anisotropic velocity distribution. Finally, the black curves are contours of constant luminous mass density in steps of one magnitude.

The density of the triaxial Abel model (solid curve) is well fitted by the triaxial Schwarzschild model (dashed curve). In both the Abel model and the fitted Schwarzschild model $\langle v_y \rangle / \sigma_{\mathrm{RMS}}$ is relatively low. The Abel model shows an increase to a value of 0.3 near the x-axis, caused by the decoupled core (Fig. 6). This enhancement is not well reproduced by the Schwarzschild model, which moreover shows a slight decrease of $\langle v_y \rangle / \sigma_{\mathrm{RMS}}$ towards the z-axis. In this region the ellipses are also rounder than in the Abel model, but towards the equatorial plane the ellipses are very similar. The orientation of the ellipses agrees over most of the (x, z)-plane. This shows that, although there is still room for improvement by refining for example the orbit sampling, the main intrinsic dynamical properties of the Abel model are recovered reasonably well.

6.3 DISTRIBUTION FUNCTION

The fitted triaxial Schwarzschild model results in a mass weight γ per orbit. These mass weights are a function of the three integrals of motion (E, I_2, I_3). In general, only the energy is exact, but for a separable potential I_2 and I_3 are also known explicitly and given by (2.5). The orbital mass weights are related to the DF $f(E, I_2, I_3)$ via the phase-space volume (see Vandervoort 1984)

$$\gamma(E, I_2, I_3) = \iiint\limits_{\mathrm{cell}} f(E, I_2, I_3) \, \Delta V(E, I_2, I_3) \, \mathrm{d}E \mathrm{d}I_2 \mathrm{d}I_3, \tag{6.3}$$

where the integration is over the cell in integral space represented by the orbit. The DF of the input Abel model is given in § 2.3. We first calculate ΔV and the integration volume, and then return to the comparison of the orbital mass weights.

6.3.1 Phase-space volume

The expression for the phase-space volume $\Delta V(E, I_2, I_3)$ can be deduced from the relations in § 7.1 of de Zeeuw (1985a). It is given by

$$\Delta V(E, I_2, I_3) = \frac{\gamma - \alpha}{2\sqrt{2}} \iiint\limits_{\Omega} \sqrt{\frac{(\lambda + \beta)(\mu + \beta)(\nu + \beta)}{[E - V_{\mathrm{eff}}(\lambda)] \, [E - V_{\mathrm{eff}}(\mu)] \, [E - V_{\mathrm{eff}}(\nu)]}}$$

$$\times \frac{(\lambda - \mu)(\mu - \nu)(\nu - \lambda) \, \mathrm{d}\lambda \, \mathrm{d}\mu \, \mathrm{d}\nu}{(\lambda + \alpha)(\lambda + \beta)(\lambda + \gamma)(\mu + \alpha)(\mu + \beta)(\mu + \gamma)(\nu + \alpha)(\nu + \beta)(\nu + \gamma)}, \tag{6.4}$$

where the effective potential V_{eff} is defined as[5]

$$V_{\mathrm{eff}}(\tau) = \frac{I_2}{\tau + \alpha} + \frac{I_3}{\tau + \gamma} + \frac{U(\tau)}{(\tau + \alpha)(\tau + \gamma)}, \tag{6.5}$$

and Ω is the configuration space volume accessible by the orbit in the triaxial separable potential that obeys the three integrals of motion (E, I_2, I_3).

Because of the separability of the equations of motion, each orbit in a triaxial separable potential can be considered as a sum of three independent motions. Each of these one-dimensional motions is either an oscillation of rotation in one of the three

---

[5] $U(\tau)$ is defined up to an arbitrary linear function, and can always be written as $-(\tau + \alpha)(\tau + \gamma)G(\tau)$, with $-G(\tau)$ the potential along the intermediate axis, so that the third term in (6.5) is well defined. The sign convention here is consistent with de Zeeuw (1985a)

orbit	I_2	E	λ	μ	ν
B	< 0	$V_{\mathrm{eff}}(-\beta)\ldots 0$	$[-\alpha, \lambda_{\max}]$	$[-\beta, \mu_{\max}]$	$[-\gamma, \nu_{\max}]$
I	< 0	$\min\left[V_{\mathrm{eff}}(\mu)\right]\ldots V_{\mathrm{eff}}(-\beta)$	$[-\alpha, \lambda_{\max}]$	$[\mu_{\min}, \mu_{\max}]$	$[-\gamma, -\beta]$
O	> 0	$\min\left[V_{\mathrm{eff}}(\lambda)\right]\ldots V_{\mathrm{eff}}(-\beta)$	$[\lambda_{\min}, \lambda_{\max}]$	$[\mu_{\min}, -\alpha]$	$[-\gamma, -\beta]$
S	> 0	$\max\left\{V_{\mathrm{eff}}(-\beta), \min\left[V_{\mathrm{eff}}(\lambda)\right]\right\}\ldots 0$	$[\lambda_{\min}, \lambda_{\max}]$	$[-\beta, -\alpha]$	$[-\gamma, \nu_{\max}]$

TABLE 1 — *Configuration space Ω for the four families of regular orbits.*

confocal ellipsoidal coordinates (λ, μ, ν), such that the configuration space volume Ω is bounded by the corresponding coordinate surfaces. The values of (λ, μ, ν) that correspond to these bounding surfaces can be found from Table 1 for the four families of regular orbits: boxes (B), inner (I) and outer (O) long-axis tubes, and short-axis (S) tubes. Whereas α, β and γ are the limits on (λ, μ, ν) set by the foci of the confocal ellipsoidal coordinate system, the other limits are the solutions of $E = V_{\mathrm{eff}}(\tau)$ (see Fig. 7 of de Zeeuw 1985a). In the case of the triaxial isochrone Stäckel potential (4.2), we can write this equation as a fourth-order polynomial in $\sqrt{\tau}$. The solutions are then the squares of three of the four roots of this polynomial (the fourth root is always negative).

For each orbit in our Schwarzschild model, we compute (E, I_2, I_3) by substituting the starting position and velocities of the orbit into the expressions (2.5). From the value of E and the sign of I_2 (while always $I_3 \geq 0$), we determine to which orbit family it belongs. The corresponding configuration space volume Ω is then given by the boundaries for λ, μ and ν in the last three columns of Table 1. The phase-space volume $\Delta V(E, I_2, I_3)$ follows by numerical evaluation of the right-hand side of eq. (6.4).

The integrand in (6.4) contains singularities at the integration limits, which can be removed for a triaxial isochrone potential. We write the integrand completely in terms of $(\sqrt{\sigma} \pm \sqrt{\tau})^{1/2}$, where $\sigma, \tau = \lambda, \mu, \nu$ or a constant value. Suppose now that the integral over λ ranges from λ_0 to λ_1 and the terms $(\sqrt{\lambda} - \sqrt{\lambda_0})^{1/2}$ and $(\sqrt{\lambda_1} - \sqrt{\lambda})^{1/2}$ appear in the denominator. The substitution $\sqrt{\lambda} = \sqrt{\lambda_0} + (\sqrt{\lambda_1} - \sqrt{\lambda_0})\sin^2\eta$ then removes both singularities since $d\lambda/[(\sqrt{\lambda} - \sqrt{\lambda_0})(\sqrt{\lambda_1} - \sqrt{\lambda})]^{1/2} = 4\sqrt{\lambda}\,d\eta$.

6.3.2 Cell in integral space

We approximate the triple integration over the cell in integral space in eq. (6.3) by the volume $\Delta E \Delta(I_{2,3})$. Here ΔE is the (logarithmic) range in E between subsequent sets of orbits at different energies (see § 6.1), with outer boundaries given by the central potential and $E = 0$. Because we do not directly sample I_2 and I_3 in our implementation of Schwarzschild's method, as their expressions are in general unknown, we cannot directly calculate the area $\Delta(I_{2,3})$. Instead, we compute the Voronoi diagram of the points in the (I_2, I_3)-plane that correspond to the starting position and velocities of each orbit, at a given energy E. An example is given in the left panel of Fig. 10. The area of the Voronoi bins approximates the area $\Delta(I_{2,3})$ for each orbit.

The four families of regular orbits are separated by two lines that follow from $I_2 = 0$ and $E = V_{\mathrm{eff}}(-\beta)$. The latter provides also part of the boundary on I_2 and I_3. The remainder is given by the positivity constraint on I_3 and by the solution of $E = V_{\mathrm{eff}}(\kappa_0)$ and $\mathrm{d}V_{\mathrm{eff}}(\kappa_0)/\mathrm{d}\kappa = 0$, with $\kappa_0 \geq -\beta$ (cf. eqs 64 and 65 of de Zeeuw 1985a).
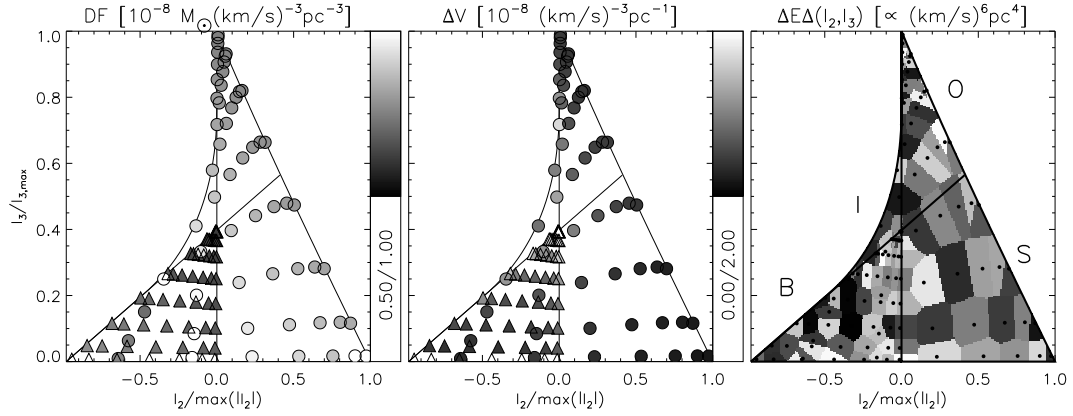
FIGURE 10 — *Three quantities involved in the calculation of the orbital mass weights for a triaxial Abel model with an isochrone potential. For a given energy E, in each panel, the values of the second and third integral of motion, I_2 and I_3, are shown that correspond to the orbital starting position and velocities in the triaxial Schwarzschild model that is fitted to the observables of this triaxial Abel model. The circles refer to orbits started in the (x, z)-plane and the triangles represent the additional set of orbits dropped from the equipotential surface (see § 6.1). The grey scale in the left panel indicates the value of the DF $f(E, I_2, I_3)$ for each orbit. The grey scale in the middle panel represents the values of the phase-space volume $\Delta V(E, I_2, I_3)$. The area of each Voronoi bin in the right panel, multiplied by the range in energy E, approximates the cell $\Delta E \Delta(I_2, I_3)$ in integral space for each orbit. The product of these three values provides an estimate of the mass weight $\gamma(E, I_2, I_3)$ for each orbit. The solid curves bound and separate the regions of the box (B) orbits, inner (I) and outer (O) long-axis tube orbits and short-axis (S) tube orbits.*

For $-\beta \leq \kappa_0 \leq -\alpha$ the solution describes the boundary curve for which $I_2 \leq 0$ and corresponds to the thin I tube orbits. For $\kappa_0 \geq -\alpha$ we find the boundary curve for which $I_2 \geq 0$, corresponding to the thin O and S tube orbits.

There are limits on the values of κ_0 depending on the value of E, and sometimes there are no valid solutions for κ_0, which implies that the corresponding tube orbits do not contribute at that energy. These limits can be obtained from the thin orbit curves in the (x, z)-plane (Fig. 8). From the expressions for the integrals of motion (2.5) in this plane, we find that the thin orbit curves follow by solving $E = U[\lambda, \kappa_0, \kappa_0]$ for I tubes and $E = U[\kappa_0, \kappa_0, \kappa]$, with $\kappa = \mu$ for O tubes and $\kappa = \nu$ for S tubes. In general these equations have to be solved numerically, but in the case of the triaxial isochrone potential (4.2), they reduce to a second order polynomial in $\sqrt{\kappa_0}$ and the solutions simply follow from the roots of the polynomial.

6.3.3 Orbital mass weight distribution

Once we have computed for each orbit the DF $f(E, I_2, I_3)$, the phase-space volume $\Delta V(E, I_2, I_3)$ and the cell $\Delta E \Delta(I_{2,3})$ in integral space (Fig. 10), its (approximate) mass weight $\gamma(E, I_2, I_3)$ follows by multiplication of these three quantities. The resulting orbital mass weight distribution of the input triaxial Abel model is shown in the top panels of Fig. 11, and that of the fitted triaxial Schwarzschild model in the bottom panels. The energy E increases from left to right, which corresponds to increasing distance from the center as is indicated by the radius R_E (in arcsec) at the top of each
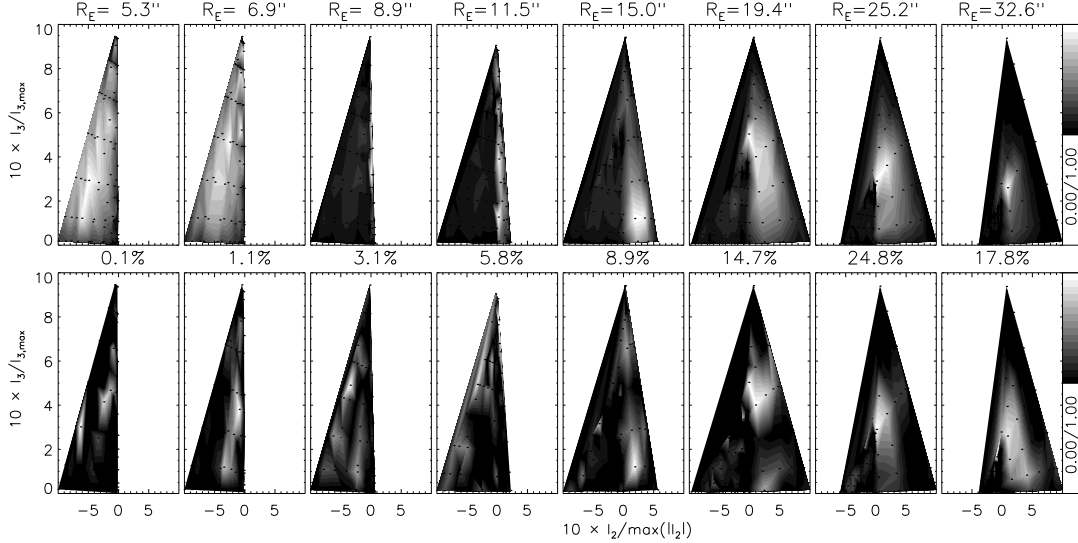
FIGURE 11 — *The orbital mass weight distribution for the input triaxial Abel model (top) and for the fitted triaxial Schwarzschild model (bottom). From left to right the energy increases, corresponding to increasing distance from the center, indicated by the radius R_E (in arcsec) of the thin short-axis tube orbit on the x-axis. The vertical and horizontal axes represent respectively the second and third integral of motion, I_2 and I_3, normalized by their maximum amplitude (for given E). Between the two rows of panels, the fraction (in %) of the included mass with respect to the total mass is indicated. (See p. 254 for a color version of this figure.)*

panel. For this representative radius we use the radius of the corresponding thin (S) tube orbit on the long x-axis (Fig. 8). The values of I_2 and I_3 on the horizontal and vertical axes respectively, are both normalized with respect to their maximum amplitude at the given energy. In each panel the mass weight values are normalized with respect to the maximum in that panel. Between the two rows of panels, the fraction of the summed values in each panel with respect to the total mass weight in all panels is given as a percentage.

The four panels with the largest fraction in mass, with R_E between about 15″ and 30″, are best constrained by the kinematic observables, taking into account that even orbits that extend beyond the maximum radius covered by the data can contribute significantly at lower radii. In these panels, the main features of the orbital mass weight distribution of the triaxial Abel model are recovered reasonably well. In the inner panels the orbital mass weight distribution in the Schwarzschild model is relatively noisy, which is mostly the consequence of the discreteness of the orbit library as well as the numerical nature of the method. In the outer parts the Schwarzschild model is still constrained by the mass model, which extends to a radius of about hundred arcseconds, but the orbital mass weight distribution deviates from that of the input Abel model due to the lack of kinematic constraints.

6.4 GLOBAL PARAMETERS

In the experiments described in the above, we computed the best-fit Schwarzschild model for the viewing angles $(\vartheta, \varphi, \psi) = (70°, 30°, 101°)$ and mass-to-light ratio $M/L =$
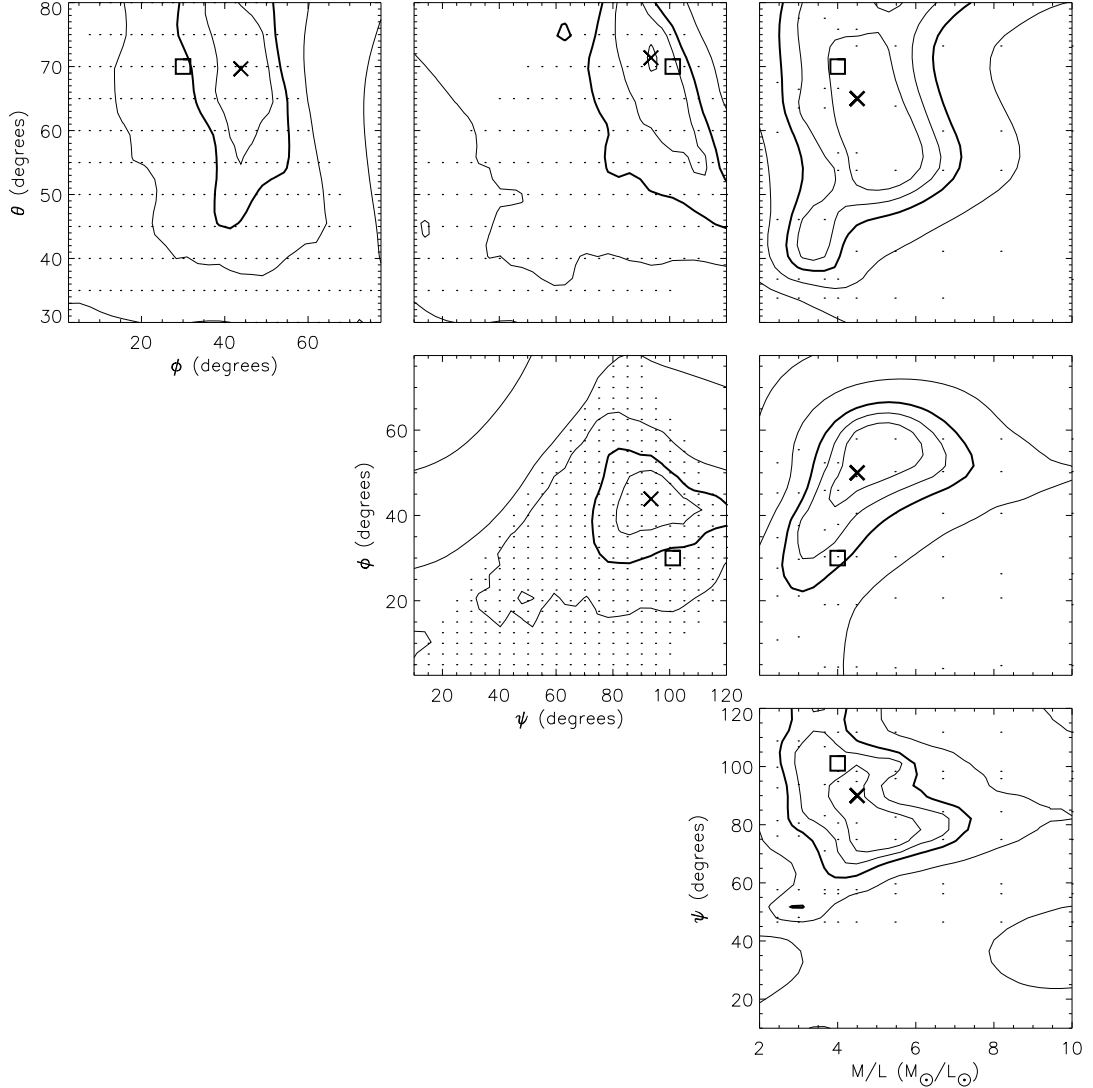
FIGURE 12 — The (marginalized) goodness-of-fit parameter $\Delta\chi^2$ as a function of viewing angles $(\vartheta, \varphi, \psi)$ and mass-to-light ratio M/L, for different triaxial Schwarzschild model fits to a triaxial Abel model (see text for details). The χ^2-values are offset such that the overall minimum, indicated by the cross, is zero. The contours are drawn at the confidence levels for a $\Delta\chi^2$-distribution with four degrees of freedom, with inner three contours corresponding to the 68.3%, 95.4% and 99.7% (thick contour) confidence levels. Subsequent contours correspond to a factor of two increase in $\Delta\chi^2$. The parameters of the input Abel model, $(\vartheta, \varphi, \psi) = (70°, 30°, 101°)$ and $M/L = 4\ M_\odot/L_\odot$, are indicated by the open square.

4 $M_\odot/L_\odot$ for which the simulated observables of the triaxial Abel model were obtained. We recalculated the best-fit Schwarzschild model for a range of these parameters, and compared the resulting χ^2-values (6.1) in order to establish which models (still) provide an acceptable fit. We quantify the quality of each fit by the difference

$\Delta\chi^2(\vartheta, \varphi, \psi, M/L)$ with respect to the overall minimum χ^2 value. To visualize this four-dimensional function, we calculate for a pair of parameters, say ϑ and φ, the minimum in $\Delta\chi^2$ as function of the remaining parameters, ψ and M/L in this case. The contour plots of the resulting marginalized $\Delta\chi^2$ for all different pairs of parameters are shown in Fig. 12. The contours are drawn at the confidence levels for a $\Delta\chi^2$-distribution with four degrees of freedom, with the inner three contours corresponding to the 68.3%, 95.4% and 99.7% (thick contour) confidence levels. Subsequent contours correspond to a factor of two increase in $\Delta\chi^2$. In each panel, the overall minimum ($\Delta\chi^2 = 0$) is indicated by the cross, while the open square corresponds to the parameters of the input Abel model.

A range of viewing angles is excluded as they lead to nonphysical deprojections of the MGE fit to the projected luminosity density (or surface brightness). Since the observables depend in a non-linear way on the viewing angles, we do not sample the viewing angles uniformly. Instead, we sample uniformly in the characteristic (4.5) axis ratios b/a, c/a and a'/a for a given observed flattening b'/a', resulting in an irregular grid in the viewing angles. In this way, we keep the number of viewing angles relatively low and still have a representative sampling. Since the Schwarzschild method is computationally expensive, such an optimization allows a full search through parameter space within a reasonable time. A parallel search on thirty desktop computers through three hundred combinations of viewing angles and ten different M/L values, currently takes about one week. To calculate the marginalized $\Delta\chi^2$ we need to interpolate (linearly) in the irregular grid of viewing angles. The dots in Fig. 12 show the corresponding (regular) grid of viewing angles, together with the (regular) sampling in M/L.

We find that the input M/L is well recovered, with a typical uncertainty of order 10 %. The viewing angles of the input model are recovered to within 10 degrees, but the allowed range in ϑ is about 35 degrees, and for φ and ψ it is almost 20 degrees. While Schwarzschild models with global parameters in this range provide an acceptable fit to the observables, their intrinsic moments and orbital mass weight distribution can deviate significantly from those of the input Abel model. We return to this apparent degeneracy in the viewing direction in § 8.

7 RECOVERY OF AXISYMMETRIC GALAXY MODELS

We now describe the application of our axisymmetric implementation of Schwarzschild's method to the observables of the oblate Abel model of § 5.3, while highlighting the differences with the above application in triaxial geometry.

7.1 AXISYMMETRIC SCHWARZSCHILD MODELS

Our implementation of Schwarzschild's method in axisymmetric geometry is described in detail in Cappellari et al. (2005). The main differences with respect to our triaxial implementation are certain simplifications due to the extra symmetry. There are no twists in the surface brightness. We use the same set-up as in the triaxial case, but since the box orbits are not present, the additional dropping of orbits from the equipotential surface is not needed.

7.2 INTRINSIC MOMENTS

It is convenient to analyze the intrinsic velocity moments of (oblate) axisymmetric models in cylindrical coordinates (R, ϕ, z). Because of axisymmetry the models are
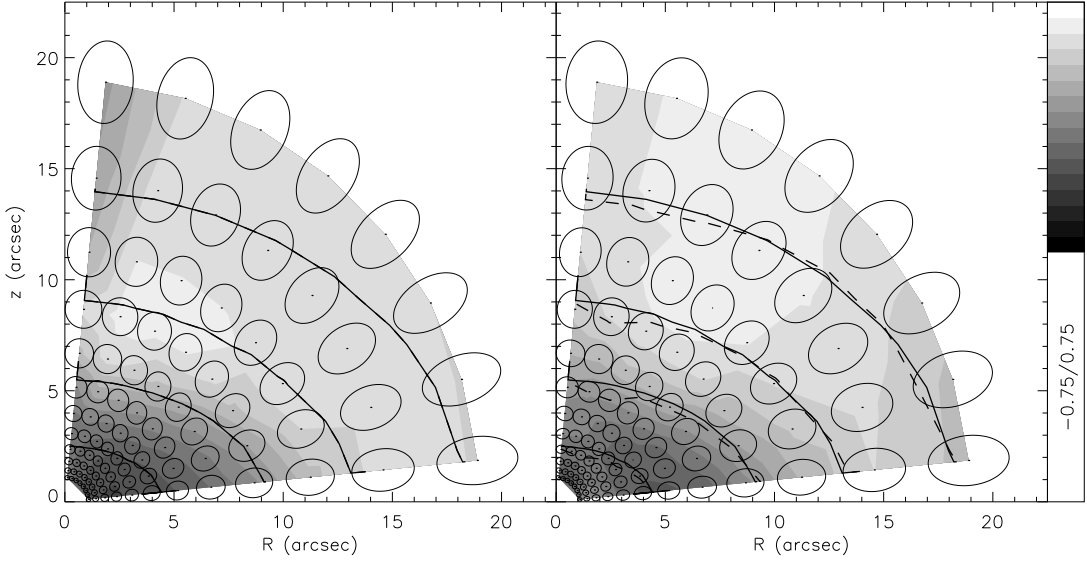
FIGURE 13 — *The mean azimuthal motion $\langle v_\phi \rangle$ perpendicular to the meridional plane, normalized by σ_{RMS}, for an oblate axisymmetric Abel model (left) and for the best-fit axisymmetric Schwarzschild model (right). Parameters and grey scale are as in Fig. 9. (See p. 255 for a color version of this figure.)*

independent of the azimuthal angle ϕ, and it is sufficient to consider the meridional (R, z)-plane. The analysis of the intrinsic velocity moments in the (R, z)-plane is similar to that for the triaxial case in the (x, z)-plane (§ 6.2). In this case, the mean azimuthal rotation $\langle v_\phi \rangle$, perpendicular to the meridional plane, is the only non-vanishing first order velocity moment. In Fig. 13, we compare the values of $\langle v_\phi \rangle / \sigma_{\mathrm{RMS}}$, indicated by the grey scale, for the Abel model (left panel) with those for the fitted Schwarzschild model (right panel). The root-mean-square velocity dispersion σ_{RMS} is defined as $\sigma_{\mathrm{RMS}}^2 = (\sigma_R^2 + \sigma_\phi^2 + \sigma_z^2)/3$. The azimuthal axis of the velocity ellipsoid, with semi-axis length σ_ϕ defined as $\sigma_\phi^2 = \langle v_\phi^2 \rangle - \langle v_\phi \rangle^2$, is perpendicular to the meridional plane. The cross sections with the meridional plane are indicated by the ellipses in Fig. 13, where the semi-axis lengths follow from (6.2) by replacing (x, z) with (R, z).

As in the triaxial case the density (solid curve) is well fitted by the axisymmetric Schwarzschild model (dashed curve). The Abel model shows a strong gradient in $\langle v_\phi \rangle / \sigma_{\mathrm{RMS}}$, which is accurately recovered by the axisymmetric Schwarzschild model. The absolute difference is on average less than 0.07, except near the symmetry z-axis. This is likely the result of numerical difficulties due to the small fraction of mass contributed in this region by the short-axis tube orbits. The shape and orientation of the ellipses are nearly identical, indicating that the anisotropic velocity distribution of the Abel model is recovered to high accuracy. The lengths of the axes of the velocity ellipsoid deviate on average by only 5 km s^{-1}, i.e., well within the typical error of 10 km s^{-1} assigned to the simulated velocity dispersion of the Abel model (§ 5.3).
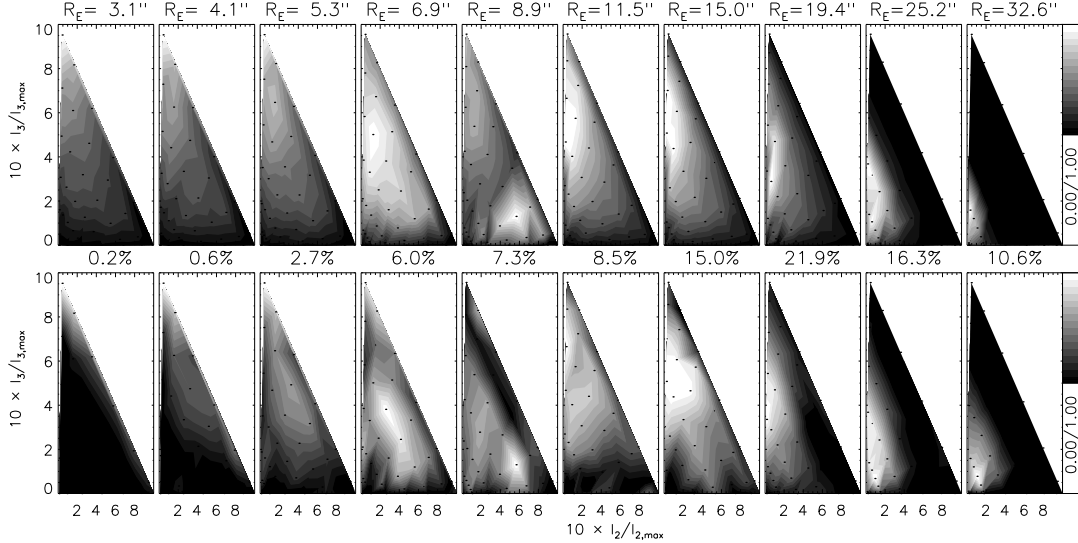
FIGURE 14 — *The mass weight distribution for an oblate axisymmetric Abel model (top) and for the fitted axisymmetric Schwarzschild model (bottom). Parameters and grey scale are the same as in Fig. 11. In this case, the second integral of motion $I_2 = \frac{1}{2}L_z^2$, where L_z is the component of the angular momentum parallel to the symmetry z-axis. (See p. 256 for a color version of this figure.)*

7.3 DISTRIBUTION FUNCTION

In the oblate axisymmetric case, all (regular) orbits are short-axis tube orbits with $I_2 = \frac{1}{2}L_z^2$ and energy E ranging from $\min[V_{\mathrm{eff}}(\lambda)]$ to zero. The expression (6.4) for the phase-space volume reduces to

$$\Delta V(E, L_z, I_3) = \frac{\pi}{2\,|L_z|} \int\limits_{-\gamma}^{\nu_{\max}} \int\limits_{\lambda_{\min}}^{\lambda_{\max}} \sqrt{\frac{(\lambda+\alpha)(\nu+\alpha)}{[E-V_{\mathrm{eff}}(\lambda)]\,[E-V_{\mathrm{eff}}(\nu)]}} \; \frac{(\nu-\lambda)\,\mathrm{d}\lambda\,\mathrm{d}\nu}{(\lambda+\alpha)(\lambda+\gamma)(\nu+\alpha)(\nu+\gamma)}, \quad (7.1)$$

where as before $\nu_{\max}$, $\lambda_{\min}$ and $\lambda_{\max}$ are the solutions of $E = V_{\mathrm{eff}}(\tau)$ (see Fig. 23 of de Zeeuw 1985a). The factor in front of the double integral includes the factor 2π from the integration over the azimuthal angle ϕ. In Fig. 14, we show in the top panels the orbital mass weight distribution of the oblate axisymmetric Abel model, and in the bottom panels that of the fitted axisymmetric Schwarzschild model.

The three-integral mass weight distributions are very similar, even in the panels with a relatively low mass content. The average fractional error is around 20 %, and if we consider in each panel the mass weights above the mean value, which together contribute nearly half of the total mass, the fractional error decreases to around 15 %. A similar good recovery was found by Krajnović et al. (2005) for the case of a two-integral DF $f(E, L_z)$, which implies an isotropic velocity distribution in the meridional plane. Thomas et al. (2005) showed that their independent axisymmetric numerical implementation of Schwarzschild's method is similarly able to recover an analytical $f(E, L_z)$. Our results show that the orbital mass weight distribution that follows from a fully three-integral DF $f(E, L_z, I_3)$ can be recovered with high accuracy as well.
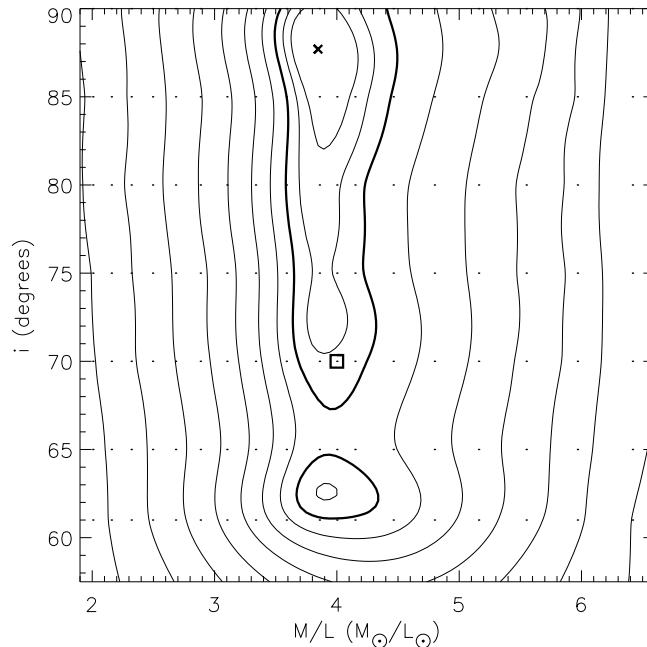
FIGURE 15 — *The goodness-of-fit parameter $\Delta\chi^2$ as a function of inclination i and mass-to-light ratio M/L, for different axisymmetric Schwarzschild model fits (indicated by the dots) to an oblate axisymmetric Abel model (see text for details). The contours are as in Fig. 12, but for a $\Delta\chi^2$-distribution with two degrees of freedom. The cross indicates the overall best-fit model ($\Delta\chi^2 = 0$). The parameters of the input Abel model, $i = 70°$ and $M/L = 4\ M_\odot/L_\odot$, are indicated by the open square.*

7.4 GLOBAL PARAMETERS

In the axisymmetric case we only have the inclination i as viewing angle, so that, together with the mass-to-light ratio, there are two global parameters. For a range of these global parameters, we fit axisymmetric Schwarzschild models to the simulated observables of the oblate axisymmetric Abel model, and compare the corresponding goodness-of-fit χ^2-values. In Fig. 15, we show the resulting differences $\Delta\chi^2$ with respect to the overall best-fit Schwarzschild model, indicated by the cross. The contours are now for a $\Delta\chi^2$-distribution with two degrees of freedom. The $M/L = 4\ \mathrm{M_\odot/L_\odot}$ of the input Abel model is recovered accurately, with an average fractional error of less than 10 %. However, for the inclination nearly all values within the allowed range by the flattening ($i > 60$) are allowed, including the value of $i = 70°$ used to compute the observables of the Abel models. Krajnović et al. (2005) and Cappellari et al. (2005) found similar evidence for a possible degeneracy in the inclination.

8 DISCUSSION AND CONCLUSIONS

We have extended the Abel models introduced by DL91 and generalized by MD99, and used them to construct realistic axisymmetric and triaxial galaxy models to test the accuracy of Schwarzschild's orbit superposition method.

Although Abel models have separable potentials with a central core and assume

a specific functional form for the (three-integral) DF, they can have a large range of shapes and their observables, which can be calculated easily, include many of the features seen in the kinematic maps of early-type galaxies. We have used an isochrone Stäckel potential that in the axisymmetric limit reduces to the Kuzmin-Kutuzov model and becomes Hénon's isochrone in the spherical limit. Because of the simple form of the isochrone potential, the resulting Abel models are ideally suited to test numerical implementations of the Schwarzschild orbit superposition method. The calculation of the phase-space volume, needed when comparing the orbital mass weight distribution of the Schwarzschild models with the three-integral DF of the Abel models, simplifies significantly for this case.

Integral-field observations in principle provide the LOSVD as a function of position on the sky, so that it is a function $\mathcal{L}(x', y', v_{z'})$ that depends on three variables. Our oblate axisymmetric and triaxial model galaxies have a DF which is a sum of Abel components $f(S) = f(-E + wI_2 + uI_3)$ with different values of the parameters w and u, so that the DF is a function of three variables as well, namely the integrals of motion E, I_2 and I_3. We have shown that by fitting Schwarzschild models to the simulated observables of these models, $f(E, I_2, I_3)$ is well recovered for the input value of the mass-to-light ratio M/L and the correct viewing angle(s). By varying these global parameters, we have found that the best-fit M/L is close to the input value, but the viewing direction is less well determined.

First consider three-integral oblate models, i.e., with a DF that is a function $f(E, L_z, I_3)$ and the viewing direction defined by the inclination. The value of M/L is recovered to within 10% for all models, but the inclination is poorly constrained. Since we assume M/L is constant, the total luminosity of the model is fixed, and the total mass follows from the virial theorem, it is not surprising that the value of M/L is insensitive to a change in inclination. If the inclination is wrong, then, in order to fit the observed surface brightness, the deprojected mass model requires a different intrinsic flattening. Our results show that there is sufficient freedom in $f(E, L_z, I_3)$ to still fit the observed (moments of) $\mathcal{L}(x', y', v_{z'})$, so that the inclination is not well-determined.

The observed ellipticity of the surface brightness places a lower limit on the inclinations that provide a physical deprojection. In some galaxies the presence of a gas or dust disk provides a further constraint. An embedded disk of stars, which is not directly visible in the observed surface brightness (e.g., Rix & White 1992), might constrain the inclination as well. This can be tested by fitting the observables of an Abel model that contains a disk-like DF component. Work along these lines is in progress.

If, instead of having a three-integral DF $f(E, L_z, I_3)$, a galaxy happens to be well approximated by a two-integral DF $f(E, L_z)$, the range of inclinations that leads to an acceptable fit of the three-parameter $\mathcal{L}(x', y', v_{z'})$ is expected to shrink. The density $\rho(R, z)$ of an axisymmetric model uniquely determines the even part of $f(E, L_z)$ and the mean streaming $\rho\langle v_\phi \rangle$ in the meridional plane fixes the part of $f(E, L_z)$ that is odd in L_z (Dejonghe 1986). Ignoring non-uniqueness in the deprojection of the surface density Σ (Rybicki 1987) and the mean streaming motion V on the plane of the sky, these two quantities define a two-integral DF completely. The observed velocity dispersion and higher moments of $\mathcal{L}(x', y', v_{z'})$ will not be fitted, except at the correct inclination. In this way, e.g. by fitting a two-integral Jeans model [i.e., solution of the Jeans equations assuming the DF is of the form $f(E, L_z)$] to the observed velocity dispersion field of a galaxy, an apparent best fit at a certain inclination can be found (e.g., Cappellari et al. 2005). However, the reliability of the derived best-fit inclination,

of course, depends on the correctness of the assumption of a two-integral DF.

In the triaxial case, the DF is again a function of three integrals of motion, but the orbital structure in these models is substantially richer than in the oblate axisymmetric models, with four major orbit families, instead of only one. This introduces a fundamental non-uniqueness in the recovery of the DF. Whereas in the oblate axisymmetric case $\rho(R, z)$ uniquely defines the even part of $f(E, L_z)$, in the (separable) triaxial case the density $\rho(x, y, z)$ does *not* uniquely determine the even part of $f(E, I_2, I_3)$, although both of these are functions of three variables (Hunter & de Zeeuw 1992). It is not known whether specification of $\mathcal{L}(x', y', v_{z'})$ can narrow down the range of possible DFs further, even ignoring the non-uniqueness caused by the required deprojection of the surface brightness. Our results show that the Schwarzschild method recovers the correct orbital mass weight distribution for the input values of the three viewing angles $(\vartheta, \varphi, \psi)$ and the mass-to-light ratio M/L. Given the very large freedom in orbit choice for this case, the modest resolution of our orbit library, and the resulting approximations in the evaluation of the phase space volume, the agreement between the orbital mass weights found in § 6.3 is in fact remarkable. It may be possible to improve the DF recovery further by refining the sampling of the orbits and the regularization of the orbital mass weights.

By varying the four global parameters, we have seen that the M/L value is again well-determined. A range of $(\vartheta, \varphi, \psi)$ is excluded as they lead to nonphysical deprojections of the observed surface brightness. In particular the presence of twists in the position angle of the isophotes can substantially constrain the viewing direction. But given the availability of four major orbit families, it is not surprising that, within the allowed space of viewing angles, there is sufficient freedom to adapt $f(E, I_2, I_3)$ to fit the observables, even if the viewing angles are wrong. This degeneracy is similar to that in the axisymmetric case. As before, in some galaxies the presence of a disk might provide a constraint on the viewing direction. Furthermore, assuming the potential is nearly separable, which might be appropriate outside the nuclear region, and use of the continuity equation (as done by Statler 1994), or the Jeans equation solutions of van de Ven et al (2003), might appear to constrain the viewing angles, but at the expense of assuming a mean streaming field or dispersion field in the (x, z)-plane. If this happens to be (very close to) the right choice, then the inferred viewing angles (and intrinsic structure) are correct, but this is not known a priori. A similar conclusion applies to model fits with a limited number of Abel DF components. By including the full range of Abel DF components, one would presumably recover the larger range of allowed viewing angles also found by Schwarzschild's method.

We conclude that Schwarzschild's method is able to recover the internal dynamical structure of early-type galaxies and allows an accurate determination of the mass-to-light ratio, but additional information is needed to constrain better the viewing direction. The axisymmetric Schwarzschild method has already been successfully applied by us and other groups to determine the black hole mass, mass-to-light ratio, dark matter profile as well as the (three-integral) DF of early-type galaxies. With our extension to triaxial geometry we are now able to model early-type galaxies — and in particular the giant ellipticals — which show clear signatures of non-axisymmetry, including isophote twist, kinematic misalignment and kinematic decoupled components. Moreover, since triaxial galaxies may appear axisymmetric (or even spherical) in projection, we can investigate the effect of intrinsic triaxiality on the measurements of e.g. black hole masses based on axisymmetric model fits to observations of galaxies.

REFERENCES

Arnold R., 1990, MNRAS, 244, 465

Arnold R., de Zeeuw P. T., Hunter C., 1994, MNRAS, 271, 924

Bacon R., et al. 2001, MNRAS, 326, 23

Batsleer P., Dejonghe H., 1993, A&A, 271, 104

Binney J., 1982, MNRAS, 201, 15

Blinnikov S., Moessner R., 1998, A&AS, 130, 193

Camm G. L., 1941, MNRAS, 101, 195

Cappellari M., 2002, MNRAS, 333, 400

Cappellari M., Copin Y., 2003, MNRAS, 342, 345

Cappellari M., et al. 2005, MNRAS, submitted, astro-ph/0505042

Cappellari M., Verolme E. K., van der Marel R. P., Verdoes Kleijn G. A., Illingworth G. D., Franx M., Carollo C. M., de Zeeuw P. T., 2002, ApJ, 578, 787

Carlson B. C., 1977, Special Functions of Applied Mathematics. Academic Press, New York San Francisco London

Carollo C. M., de Zeeuw P. T., van der Marel R. P., 1995, MNRAS, 276, 1131

Chandrasekhar S., 1940, ApJ, 92, 441

Copin Y., Cretton N., Emsellem E., 2004, A&A, 415, 889

Cretton N., de Zeeuw P. T., van der Marel R. P., Rix H., 1999, ApJS, 124, 383

Cretton N., Emsellem E., 2004, MNRAS, 347, L31

Cretton N., Rix H.-W., de Zeeuw P. T., 2000, ApJ, 536, 319

Cretton N., van den Bosch F. C., 1999, ApJ, 514, 704

Davies R. L., et al. 2001, ApJ, 548, L33

de Zeeuw P. T., 1985a, MNRAS, 216, 273

de Zeeuw P. T., 1985b, MNRAS, 216, 599

de Zeeuw P. T., Franx M., 1989, ApJ, 343, 617

de Zeeuw P. T., Hunter C., Schwarzschild M., 1987, ApJ, 317, 607

de Zeeuw P. T., Lynden-Bell D., 1985, MNRAS, 215, 713

de Zeeuw P. T., Peletier R., Franx M., 1986, MNRAS, 221, 1001

de Zeeuw P. T., Pfenniger D., 1988, MNRAS, 235, 949

Dejonghe H., 1986, Phys. Rep., 133, 217

Dejonghe H., de Zeeuw P. T., 1988, ApJ, 333, 90

Dejonghe H., Laurent D., 1991, MNRAS, 252, 606 [DL91]

Eddington A. S., 1915, MNRAS, 76, 37

Eddington A. S., 1916, MNRAS, 76, 572

Edgeworth F. Y., 1905, Cambridge Philos. Soc., 20, 36

Emsellem E., et al. 2004, MNRAS, 352, 721

Franx M., 1988, MNRAS, 231, 285

Gebhardt K., et al. 2000, AJ, 119, 1157

Gebhardt K., et al. 2003, ApJ, 583, 92

Gerhard O. E., 1993, MNRAS, 265, 213

Gradshteyn I. S., Ryzhik I. M., 1994, Table of Integrals, Series and Products. Academic Press, San Diego

Henon M., 1959, Annales d'Astrophysique, 22, 126

Hunter C., de Zeeuw P. T., 1992, ApJ, 389, 79

Jeans J. H., 1915, MNRAS, 76, 70

Kauffmann G., van den Bosch F., 2002, Scientific American, 286, 36

Krajnović D., Cappellari M., Emsellem E., McDermid R. M., de Zeeuw P. T., 2005, MNRAS, 357, 1113

Kuzmin G. G., 1973, in Proc. All-Union Conf., Dynamics of Galaxies and Clusters. ed. T. B. Omarov (Alma Ata: Akad. Nauk Kazakhskoj SSR), 71 (English transl. in IAU Symp. 127, Structure and Dynamics of Ell. Galaxies, ed. P.T. de Zeeuw [Dordrecht: Reidel], 553)

Kuzmin G. G., Kutuzov S. A., 1962, Bull. Abastumani Astroph. Obs., 27, 82

Lynden-Bell D., 1962, MNRAS, 124, 1

Mathieu A., Dejonghe H., 1996, A&A, 314, 25

Mathieu A., Dejonghe H., 1999, MNRAS, 303, 455 [MD99]

Mathieu A., Dejonghe H., Hui X., 1996, A&A, 309, 30

Merritt D., 1985, AJ, 90, 1027

Navarro J. F., Frenk C. S., White S. D. M., 1997, ApJ, 490, 493

Osipkov L. P., 1979, Pis'ma v Astronomicheskii Zhurnal, 5, 77

Pfenniger D., 1984, A&A, 134, 373

Primack J. R., 2004, in IAU Symp. 220: Dark Matter in Galaxies, eds. S. D. Ryder, D. J. Pisano, M. A. Walker, and K. C. Freeman, p. 53

Richstone D. O., Tremaine S., 1984, ApJ, 286, 27

Rix H., de Zeeuw P. T., Cretton N., van der Marel R. P., Carollo C. M., 1997, ApJ, 488, 702

Rix H.-W., White S. D. M., 1992, MNRAS, 254, 389

Romanowsky A. J., Douglas N. G., Arnaboldi M., Kuijken K., Merrifield M. R., Napolitano N. R., Capaccioli M., Freeman K. C., 2003, Science, 301, 1696

Rybicki G. B., 1987, in IAU Symp. 127: Structure and Dynamics of Elliptical Galaxies, ed. P. T. de Zeeuw, p. 397

Schwarzschild M., 1979, ApJ, 232, 236

Schwarzschild M., 1982, ApJ, 263, 599

Schwarzschild M., 1993, ApJ, 409, 563

Scorza C., Bender R., 1995, A&A, 293, 20

Statler T. S., 1987, ApJ, 321, 113

Statler T. S., 1991, AJ, 102, 882

Statler T. S., 1994, ApJ, 425, 458

Statler T. S., Emsellem E., Peletier R. F., Bacon R., 2004, MNRAS, 353, 1

Teuben P., 1987, MNRAS, 227, 815

Thomas J., Saglia R. P., Bender R., Thomas D., Gebhardt K., Magorrian J., Corsini E. M., Wegner G., 2005, MNRAS, 360, 1355

Thomas J., Saglia R. P., Bender R., Thomas D., Gebhardt K., Magorrian J., Richstone D., 2004, MNRAS, 353, 391

Treu T., Koopmans L. V. E., 2004, ApJ, 611, 739

Valluri M., Merritt D., Emsellem E., 2004, ApJ, 602, 66

van Albada T. S., Bahcall J. N., Begeman K., Sancisi R., 1985, ApJ, 295, 305

van de Ven G., Hunter C., Verolme E. K., de Zeeuw P. T., 2003, MNRAS, 342, 1056 (Chapter 5)

van de Ven G., van den Bosch R. C. E., Verolme E. K., de Zeeuw P. T., 2005, A&A, in press, astro-ph/0509228 (Chapter 2)

van den Bosch R. C. E., van de Ven G., Verolme E. K., Cappellari M., de Zeeuw P. T., 2006, MNRAS, to be submitted

van der Marel R. P., Cretton N., de Zeeuw P. T., Rix H., 1998, ApJ, 493, 613

van der Marel R. P., de Zeeuw P., Rix H.-W., Quinlan G. D., 1997, Nature, 385, 610

van der Marel R. P., Franx M., 1993, ApJ, 407, 525

Vandervoort P. O., 1984, ApJ, 287, 475

Verolme E. K., de Zeeuw P. T., 2002, MNRAS, 331, 959

Verolme E. K., et al. 2002, MNRAS, 335, 517

Verolme E. K., et al. 2003, in Galaxies and Chaos, eds. G. Contopoulos and N. Voglis, LNP vol. 626, p. 279

Weinacht J., 1924, Math. Ann., 91, 279

APPENDIX A LIMITING CASES

When two or all three of the constants α, β or γ that define the confocal coordinate system are equal, the triaxial Abel models reduce to limiting cases with more symmetry and thus with fewer degrees of freedom. The oblate and prolate axisymmetric limits are described in § 5.1. DL91 derived the non-rotating Abel models for elliptic disks and in the spherical limit. We summarize their results and give the rotating

Abel models for these limiting cases. At the same time, we also derive the properties of the non-rotating and rotating Abel models in the limit of large radii.

A.1   ELLIPTIC DISK POTENTIAL

The two-dimensional analogues of the triaxial Abel models are the elliptic Abel disks with Stäckel potential $V_S(\lambda, \mu) = U[\lambda, \mu]$ in confocal elliptic coordinates (λ, μ). The relations with (x, y) follow from those in § 2.1 by setting $z = 0$ and $\nu = -\beta = -\gamma$. Choosing the DF as $f(E, I_2) = f(S)$, with $S = -E + w I_2$, with the two integrals of motion

$$E = \tfrac{1}{2} \left(v_x^2 + v_y^2 \right) + U[\lambda, \mu], \quad I_2 = \tfrac{1}{2} L_x^2 + \tfrac{1}{2}(\beta - \alpha)v_x^2 + (\beta - \alpha)x^2 U[\lambda, \mu, -\alpha], \qquad (A.1)$$

the velocity moments can be evaluated as

$$\mu_{lm}(\lambda, \mu) = \sqrt{\frac{2^{l+m+2}}{[1-(\lambda+\alpha)w]^{l+1}[1-(\mu+\alpha)w]^{m+1}}} \int\limits_{S_{\min}}^{S_{\max}} T_{mn} \left[S_{\text{top}}(\lambda, \mu) - S \right]^{(l+m)/2} f(S) \, \mathrm{d}S, \quad (A.2)$$

As in the general triaxial case, $S_{\min} \geq S_{\lim}$, where the expression of the latter is given along the w-axis ($u = 0$) in Fig. 2. The accessible part of the (E, I_2)-integral space is now a triangle, the top of which is $S_{\text{top}}(\lambda, \mu) = -U[\lambda, \mu] + w(\lambda + \alpha)(\mu + \alpha)U[\lambda, \mu, -\alpha]$.

For the NR part $S_{\max} = S_{\text{top}}(\lambda, \mu)$ and $T_{lm}^{\text{NR}} = B(\frac{l+1}{2}, \frac{m+1}{2})$. Of the two possible orbit families, the box orbits have no net rotation and the tube orbits rotate around the axis perpendicular to the disk (the z-axis). Since this is similar to the short-axis tube orbits in the general triaxial case, we refer to the rotating part as the SR part. This SR part reaches the region of the accessible integral space (the triangle) for which $v_\mu^2 \geq 0$ at $\mu = -\alpha$ (or $I_2 \geq 0$). Therefore, $S_{\max} = S_{\text{top}}(\lambda, -\alpha)$ and

$$T_{lm}^{\text{SR}} = 2 \int_0^{\arcsin(\sqrt{a_0})} \sin^l \theta \cos^m \theta \, d\theta, \quad a_0 = \frac{(\lambda + \alpha) \left[1 - (\mu + \alpha)w\right] \left[S_{\text{top}}(\lambda, -\alpha) - S\right]}{(\lambda - \mu) \left[S_{\text{top}}(\lambda, \mu) - S\right]}. \qquad (A.3)$$

The integral can be evaluated in terms of elementary functions (see e.g. Gradshteyn & Ryzhik 1994, relations 2.513 on p.160–162).

The NR velocity moments $\mu_{lm}^{\text{NR}}(\lambda, \mu)$ vanish when either l or m is odd, and the SR velocity moments $\mu_{lm}^{\text{SR}}(\lambda, \mu)$ only when l is odd. The latter should be multiplied with $(-1)^m$ for net rotation in the opposite direction. Further information on elliptic Stäckel disks can be found in Teuben (1987) and de Zeeuw, Hunter & Schwarzschild (1987).

A.2   LARGE DISTANCE LIMIT

At large radii, $\lambda \to r^2 \gg -\alpha$, so that the confocal ellipsoidal coordinates of § 2.1 reduce to conical coordinates (r, μ, ν), with r the usual distance to the origin, i.e., $r^2 = x^2 + y^2 + z^2$ and μ and ν angular coordinates on the sphere. In these coordinates the Stäckel potential is of the form $V_S(r, \mu, \nu) = V(r) + U[\mu, \nu]/r^2$, where $V(r)$ is an arbitrary smooth function of r. The corresponding integrals of motion are given by

$$\begin{aligned}
E &= \tfrac{1}{2} \left(v_x^2 + v_y^2 + v_z^2 \right) + V_S(r, \mu, \nu), \\
I_2 &= \tfrac{1}{2} T L_y^2 + \tfrac{1}{2} L_z^2 - (\beta - \alpha)\tfrac{x^2}{r^2} U[\mu, \nu, -\alpha], \\
I_3 &= \tfrac{1}{2} L_x^2 + \tfrac{1}{2}(1 - T)L_y^2 + (\gamma - \beta)\tfrac{z^2}{r^2} U[\mu, \nu, -\gamma].
\end{aligned} \qquad (A.4)$$

With the choice (2.9) for the DF, the expression for the velocity moments becomes

$$\mu_{lmn}(r,\mu,\nu) = \frac{1}{r^{m+n+2}} \sqrt{\frac{2^{l+m+n+3}}{F_\nu^{m+1} F_\mu^{n+1}}} \int\limits_{S_{\min}}^{S_{\max}} T_{lmn} \, [S_{\text{top}}(r,\mu,\nu) - S]^{(l+m+n+1)/2} \, f(S) \, \mathrm{d}S, \quad \text{(A.5)}$$

where F_μ and F_ν are defined as

$$F_\tau = \frac{1}{r^2} + \frac{(\tau+\alpha)\,w - (\tau+\gamma)\,u}{\gamma - \alpha}, \quad \tau = \mu, \nu. \quad \text{(A.6)}$$

As in the general triaxial case, $S_{\min} \geq S_{\lim}$, where $S_{\lim}$ can be obtained from Fig. 2. The expressions of $S_{\max}$ and T_{lmn} for the NR, LR and SR parts are those given in §§ 2.3.2–2.3.4 respectively, but with $S_{\text{top}}(\lambda,\mu,\nu)$ (eq. 2.14) replaced by

$$S_{\text{top}}(r,\mu,\nu) = -V_S(r,\mu,\nu) - w\,\frac{(\mu+\alpha)(\nu+\alpha)}{\gamma-\alpha}\,U[\mu,\nu,-\alpha] - u\,\frac{(\mu+\gamma)(\nu+\gamma)}{\alpha-\gamma}\,U[\mu,\nu,-\gamma] \quad \text{(A.7)}$$

and the parameters a_0 and b_0 (2.17) reduce to

$$a_0 = \frac{S_{\text{top}}(r,\mu,-\beta) - S}{S_{\text{top}}(r,\mu,\nu) - S}, \quad b_0 = \frac{(\mu+\beta)\,F_\nu\,[S_{\text{top}}(r,\mu,-\beta) - S]}{(\mu-\nu)\,F_{(-\beta)}\,[S_{\text{top}}(r,\mu,\nu) - S]}, \quad \text{(A.8)}$$

which by interchanging $\nu \leftrightarrow \mu$ become a_1 and b_1, and in turn a_2 and b_2 follow by $\beta \leftrightarrow \alpha$. The conversion to observables follows from § 3, with v_λ replaced by v_r and in the matrix $\mathbf{Q}$ all terms $\lambda+\sigma$ ($\sigma = -\alpha, -\beta, -\gamma, \mu, \nu$) cancel out (cf. eq. 25 of Statler 1994).

Suppose now that at large radii r, the function $V(r)$ in the Stäckel potential decreases and we keep in the above expressions only the dominant terms. In this case, F_μ, F_ν and S_{top} reduce to functions of μ and ν only. As a result, the velocity moments (A.5) are independent of r, except for the prefactor $1/r^{m+n+2}$, and therefore are scale-free. Once we have calculated the velocity moments at a radius r, those at radius $r' = qr$, with q a constant, follow by a simple scaling, $\mu_{lmn}(r',\mu,\nu) = \mu_{lmn}(r,\mu,\nu)/q^{m+n+2}$.

A.3 SPHERICAL POTENTIAL

When $\alpha = \beta = \gamma$, both μ and ν loose their meaning and we replace them by the customary polar angle θ and azimuthal angle ϕ. The expressions for the Abel models in these spherical coordinates (r,θ,ϕ) follow in a straightforward way from those in § A.2 for the large distance limit in conical coordinates (r,μ,ν).

The Stäckel potential $V_S = V(r)$ is spherical symmetric. The expressions for the integrals of motion follow from (A.4), where for I_2 and I_3 the right-most terms vanish. The triaxiality parameter T is now a free parameter, so that, together with the parameters w and u, we can rewrite $S = -E + w\,I_2 + u\,I_3$ as

$$S = -E + \tfrac{1}{2}uL_x^2 + \tfrac{1}{2}[(1-T)u + Tw]L_y^2 + \tfrac{1}{2}wL_z^2. \quad \text{(A.9)}$$

This means that with the choice (2.9) for the DF, we cover the most general homogeneous quadratic form in the velocities that is allowed by the integrals of motion in a spherical symmetric potential, i.e., the energy E and all three components of the angular momentum vector $\mathbf{L}$ (cf. DL91). These include the models considered by Osipkov (1979) and Merritt (1985) with the DF of the from $f(E \pm L^2/r_a^2)$ and those studied by

Arnold (1990) with a more general DF of the form $f(E \pm L^2/r_a^2 \pm L_z^2/r_b^2)$. These models follow by setting $u = \pm 2/r_a^2$, and $w = u$ or $w = u \pm 2/r_b^2$ respectively.

The velocity moments follow from eq. (A.5), with

$$F_\tau = \tfrac{1}{2}(w - u)\left[\cos^2\theta + T(\sin^2\theta\sin^2\phi - 1) \pm \sqrt{\Lambda}\right] - \tfrac{1}{2}(w + u) + \tfrac{1}{r^2}. \qquad \text{(A.10)}$$

where the positive and negative sign are for F_μ and F_ν respectively, and

$$\Lambda = \left[\sin^2\theta + T(\sin^2\theta\sin^2\phi - 1)\right]^2 + 4T\sin^2\theta\cos^2\theta\sin^2\phi. \qquad \text{(A.11)}$$

Taking $\alpha = \beta = \gamma$ in Fig. 2, we see that the boundaries on w and u both vanish. The separatrices L_1 and L_2, defined in eq. (2.13), reduce to the negative w-axis and the line $w = u$, respectively. Furthermore, $S_{\max} = S_{\text{top}} = V(r)$, and for T_{lmn} we use the expression (2.15). The resulting velocity moments $\mu_{lmn}(r, \theta, \phi)$, which are in general not spherical symmetric, vanish when either l, m or n is odd.

The latter implies no net rotation, which is the case when the (conserved) angular momentum vectors $\mathbf{L}$ for the orbits are randomly oriented. We can introduce net rotation if we assume that (a fraction of) the orbits have a preferred sense of rotation around an angular momentum vector $\mathbf{L}_0$ that points in a specific direction given by θ_0 and ϕ_0. Using the projection matrix P in § 3.1 with $\vartheta = \theta_0$ and $\varphi = \phi_0$, we transform to the coordinate system $(r' = r, \theta', \phi')$, in which $\mathbf{L}_0$ is aligned with the z'-axis. If we next set the DF to zero for $L_{z'} < 0$, we find $\mu'_{lmn}(r, \theta', \phi') = \tfrac{1}{2}\mu_{lmn}(r, \theta', \phi')$, which does still vanish when l or m is odd, but is non-zero when n is odd, resulting in net rotation (and after multiplication with $(-1)^n$ in opposite direction). With the inverse of the projection matrix, we can then transform these velocity moments to the original coordinates system (r, θ, ϕ). In this way, we can build spherical Abel models, which in addition to a non-rotating part consist of a component or several components with a preferred rotation axis. Mathieu, Dejonghe & Hui (1996) used this approach to construct a spherical model of Centaurus A, including DF components with rotation around the apparent long and short axis.

APPENDIX B   THE FUNCTION $\mathcal{M}(s, i, j; a, b, \phi)$

The function $\mathcal{M}$ that appears in the velocity moments of the rotating Abel components is defined as

$$\mathcal{M}(s, i, j; a, b, \phi) = \int\limits_0^\phi \left(\frac{\partial}{\partial a}\right)^i \left(\frac{\partial}{\partial b}\right)^j \frac{\left[1 - \sqrt{[1 - p(\theta)]^{s+1}}\right]}{p(\theta)}\, d\theta, \qquad \text{(B.1)}$$

with $p(\theta) \equiv a\cos^2\theta + b\sin^2\theta$. For odd s, corresponding to odd velocity moments, the integral can be evaluated in a straightforward way in terms of elementary functions. In Table B.1, we give the resulting expressions for $s = 1, 3, 5$.

For even s, the integral can be evaluated in terms of the (incomplete) elliptic integrals. To simplify the numerical evaluation we use Carlson's (1977) symmetrical forms R_F, R_D and R_J (for the relations between both forms see e.g. de Zeeuw & Pfenniger 1988). In Table B.2, we give the expressions for $s = 0, 2, 4$, where we have introduced

$s\,i\,j$	$\mathcal{M}(s, i, j; a, b, \phi)$
100	ϕ
300	$\frac{1}{2}(4 - a - b)\,\phi + \frac{1}{4}(b - a)\sin 2\phi$
310	$-\frac{1}{2}\phi - \frac{1}{4}\sin 2\phi$
301	$-\frac{1}{2}\phi + \frac{1}{4}\sin 2\phi$
500	$\frac{1}{8}(24 - 12a - 12b + 3a^2 + 3b^2 + 2ab)\,\phi$
	$+\frac{1}{4}(b - a)(3 - a - b)\sin 2\phi + \frac{1}{32}(b - a)^2 \sin 4\phi$
510	$-\frac{1}{4}(6 - 3a - b)\,\phi - \frac{1}{4}(3 - 2a)\sin 2\phi - \frac{1}{16}(b - a)\sin 4\phi$
501	$-\frac{1}{4}(6 - 3b - a)\,\phi + \frac{1}{4}(3 - 2b)\sin 2\phi + \frac{1}{16}(b - a)\sin 4\phi$
520	$\frac{3}{4}\phi + \frac{1}{2}\sin 2\phi + \frac{1}{16}\sin 4\phi$
511	$\frac{1}{4}\phi - \frac{1}{16}\sin 4\phi$
502	$\frac{3}{4}\phi - \frac{1}{2}\sin 2\phi + \frac{1}{16}\sin 4\phi$

TABLE B.1 — *The function $\mathcal{M}$ for odd s.*

the following quantities based on these symmetric elliptic integrals

$$
\begin{aligned}
F &= \frac{\sqrt{1 - a}\,\sin\phi}{a} R_F(\cos^2\phi, \Delta^2, 1), \\
D &= \frac{\sin^3\phi}{3\sqrt{1 - a}} R_D(\cos^2\phi, \Delta^2, 1), \\
J &= \frac{(b - a)\sin^3\phi}{3a^2\sqrt{1 - a}} R_J(\cos^2\phi, \Delta^2, 1, \frac{p(\phi)}{a}),
\end{aligned}
\tag{B.2}
$$

with $\Delta^2 = [1 - p(\phi)]/(1 - a)$, and we have defined the terms

$$
\begin{aligned}
A &= \frac{1}{\sqrt{ab}} \arctan\left(\sqrt{\frac{b}{a}}\tan\phi\right), \\
P &= \sin\phi\cos\phi\sqrt{1 - p(\phi)}, \\
Q &= \sin\phi\cos\phi\,\frac{1 - \sqrt{1 - p(\phi)}}{p(\phi)}.
\end{aligned}
\tag{B.3}
$$

In Fig. B.1, we show the $\mathcal{M}(s, i, j; a, b, \phi)$ as function of ϕ for the case that $a = 0.5$ and $b = 0.8$, up to order $s = 5$.

We now consider some special cases. When either a or b is zero, the corresponding velocity moments vanish (eqs 2.16 and 2.19), and when $a_i > b_i$ the arguments of the function $\mathcal{M}$ are interchanged (eqs 2.18, 2.20 and 2.21). This means we only have to consider the range $0 < a \leq b$, together with $0 < \phi \leq \pi/2$, since $\mathcal{M}$ vanishes when $\phi = 0$.

When $a = b$, it follows that $p(\theta) = a$ in eq. (B.1), and henceforth we can separate $\mathcal{M}(s, i, j; a, a, \phi) = \mathcal{M}_1(s, i, j; a)\,\mathcal{M}_2(i, j; \phi)$, where

$$
\mathcal{M}_1(s, i, j; a) = \frac{\mathrm{d}^{i+j}}{\mathrm{d}a^{i+j}}\frac{\left[1 - \sqrt{(1 - a)^{s+1}}\right]}{a}, \quad \mathcal{M}_2(i, j; \phi) = \int_0^\phi \cos^{2i}\theta \sin^{2j}\theta\,\mathrm{d}\theta.
\tag{B.4}
$$

$s\,i\,j$	$\mathcal{M}(s,i,j;a,b,\phi)$
000	$A - F + J$
200	$A - (1-a)\,F - (b-a)\,D + J$
210	$-\frac{1}{2a}\left[A + Q - (1+a)\,F + (1-a)\,D + J\right]$
201	$-\frac{1}{2b}\left[A - Q - F - (1-b)\,D + J\right]$
400	$A + \frac{1}{3}(b-a)\,P - \frac{1}{3}(2a^2 + ab - 6a + 3)\,F + \frac{1}{3}(2a+2b-7)(b-a)\,D + J$
410	$-\frac{1}{2a}\left[A + a\,P + Q - (1+2a)(1-a)\,F + (2a^2 - 2a - ab + 1)\,D + J\right]$
401	$-\frac{1}{2b}\left[A - b\,P - Q - (1-ab)\,F - (2b^2 - 2b - ab + 1)\,D + J\right]$
420	$\frac{3}{4a^2}\left\{A + \frac{a^2\,p(\phi)-ab}{3(b-a)p(\phi)}\,P + \frac{5a\cos^2\phi+3b\sin^2\phi}{3p(\phi)}\,Q + \frac{2a^3-3a^2b+4a^2+3a-3ab-3b}{3(b-a)}\,F\right.$ $\left. - \frac{(2a^2+5a-4ab-3b)(1-a)}{3(b-a)}\,D + J\right\}$
411	$\frac{1}{4ab}\left\{A + \frac{ab-ab\,p(\phi)}{(b-a)p(\phi)}\,P + \frac{b\sin^2\phi-a\cos^2\phi}{p(\phi)}\,Q + \frac{a^2b-ab+a-b}{b-a}\,F + \frac{a^2b+ab^2-4ab+a+b}{b-a}\,D + J\right\}$
402	$\frac{3}{4b^2}\left\{A + \frac{b^2\,p(\phi)-ab}{3(b-a)p(\phi)}\,P - \frac{3a\cos^2\phi+5b\sin^2\phi}{3p(\phi)}\,Q - \frac{3b-3a-ab+ab^2}{3(b-a)}\,F\right.$ $\left. - \frac{(2b^2+5b-4ab-3a)(1-b)}{3(b-a)}\,D + J\right\}$

TABLE B.2 — *The function $\mathcal{M}$ for even s.*

For $a = 1$, the expression for $\mathcal{M}_1$ simplifies to $(-1)^{i+j}(i+j)!$. The integral in the expression for $\mathcal{M}_2$ can be evaluated explicitly using e.g. the relations 2.513 of Gradshteyn & Ryzhik (1994). For $\phi = \pi/2$, it reduces to the beta function $B(i + 1/2, j + 1/2)$.

When $a < b = 1$, the elliptic integrals become elementary, so that the quantities F, D and J in eq. (B.2) reduce to

$$F = \frac{\sqrt{1-a}}{a}\,\ln\left[\tan\left(\frac{\pi}{4} + \frac{\phi}{2}\right)\right], \quad D = \frac{a}{1-a}\,F - \frac{\sin\phi}{\sqrt{1-a}}, \quad J = F - \frac{1}{\sqrt{a}}\,\arctan\left(\sqrt{\frac{1-a}{a}}\,\sin\phi\right). \quad \text{(B.5)}$$

Although F diverges when $\phi \to \pi/2$, substitution of these reduced quantities in the expressions of $\mathcal{M}$ for even s (Table B.2), shows that all terms with F cancel. For $\phi = \pi/2$, the function $\mathcal{M}$ is thus everywhere finite, with $A = \pi/(2\sqrt{ab})$ and $P = Q = 0$.

APPENDIX C   CONVERSION FROM TRUE MOMENTS TO GAUSS-HERMITE MOMENTS

We describe the conversion from the true moments of a line-of-sight velocity distribution (LOSVD) to the moments of its expansion as a Gauss-Hermite series. These Gauss-Hermite moments are used to parameterize observed LOSVDs as they are less sensitive to the often noise-dominated wings than the true moments. Because there is no simple (analytic) relation between both, we convert the projected true moments of the Abel distribution function (3.12) to Gauss-Hermite moments numerically.

One possible way is to proceed as follows: For a given set of Gauss-Hermite moments $\{\Sigma_{\mathrm{GH}}, V_{\mathrm{GH}}, \sigma_{\mathrm{GH}}, h_3, h_4, \ldots, h_N\}$ construct the corresponding LOSVD $\mathcal{L}_N^{\mathrm{GH}}(v)$ (using e.g. eq. 9 of van der Marel & Franx 1993), and (numerically) calculate its moments $\mu_k^{\mathrm{GH}} = \int_{-\infty}^{\infty} v^k \mathcal{L}_N^{\mathrm{GH}}(v)\,\mathrm{d}v$. Then find the set of Gauss-Hermite moments for which μ_k^{GH}
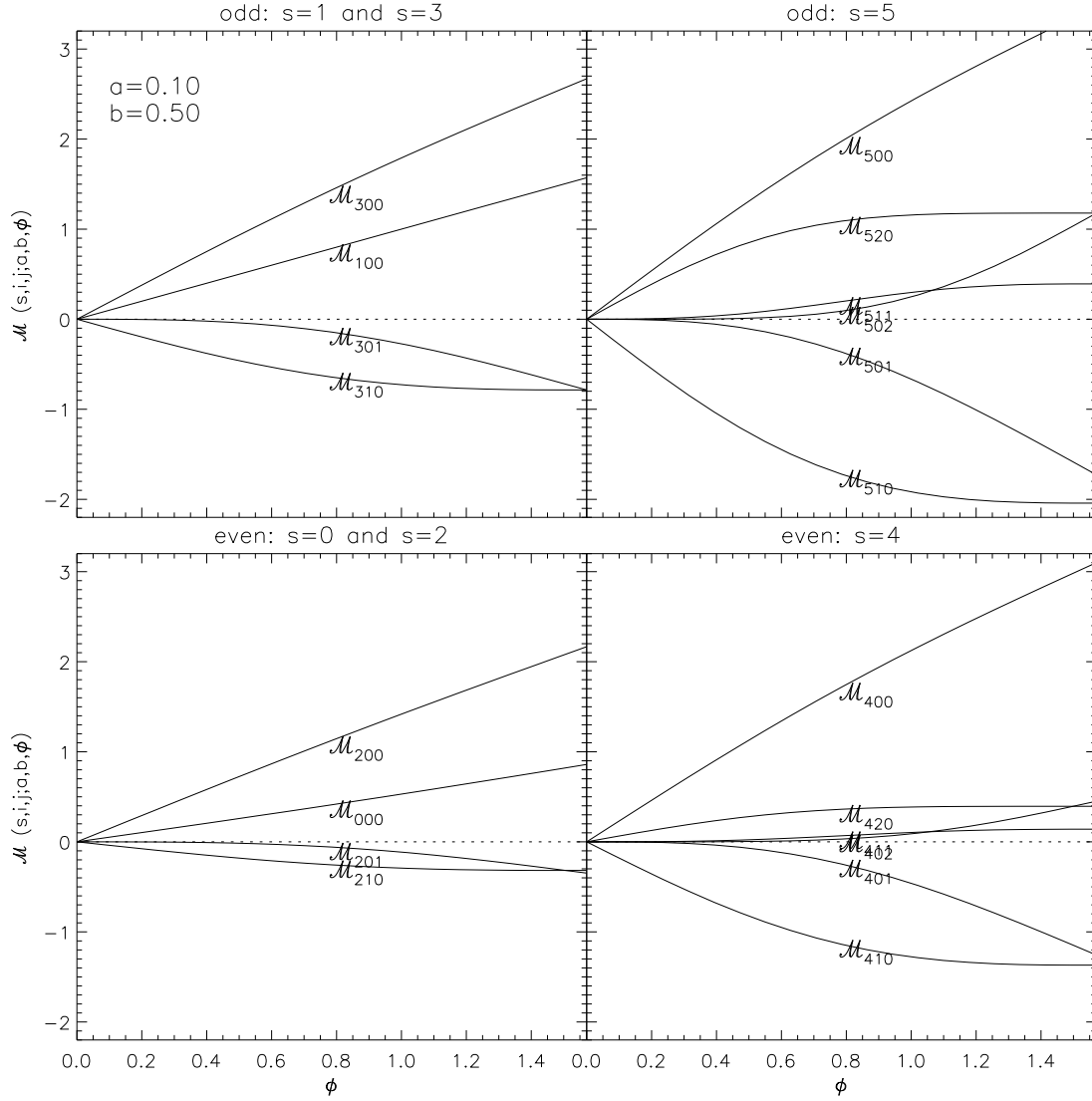
FIGURE B.1 — *The function* $\mathcal{M}(s, i, j; a, b, \phi)$ *defined in eq.* (B.1) *plotted against* ϕ, *for* $a = 0.5$ *and* $b = 0.8$, *up to order* $s = 5$. *The curves in the top panels are for odd values of* s *corresponding to the odd velocity moments, whereas the curves in the bottom panels are for even values of* s. *The indices of the labels* $\mathcal{M}_{sij}$ *refer to the first three parameters of the function* $\mathcal{M}$.

($k = 0, \ldots, K$) best fit the K true moments μ_k (3.12). This fit can be done e.g. by minimizing $\chi^2 = \sum_{k=1}^{K} \left[(\mu_k - \mu_k^{\mathrm{GH}})/(\Sigma \, \sigma^k) \right]^2$. A good initial start for the set of Gauss-Hermite moments is to set the lower-order moments equal to the true moments, $\Sigma_{\mathrm{GH}} = \Sigma$, $V_{\mathrm{GH}} = V$, $\sigma_{\mathrm{GH}} = \sigma$, and the higher order moments h_3, h_4, $\ldots$, h_N to zero.

However, in practice several problems occur with the above direct fitting of the true moments. As illustrated in the right panel of Fig. C.1, the goodness-of-fit parameter χ^2 shows (many) local minima. This means it is very hard for a minimization routine to find the global minimum. It can take long before the routine converges and even
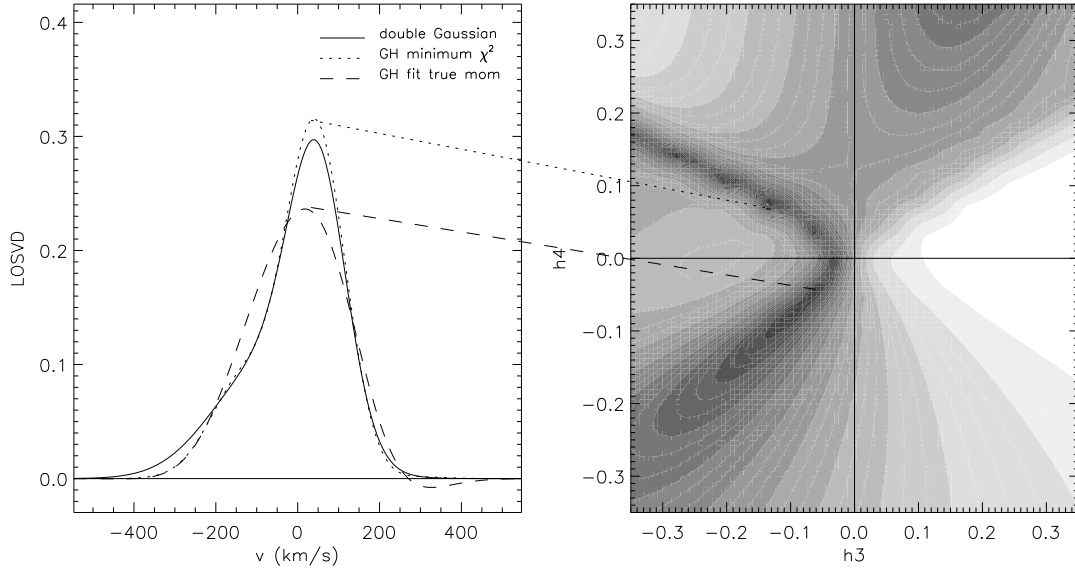
FIGURE C.1 — *Derivation of the Gauss-Hermite moments of the Scorza & Bender (1995) LOSVD by fitting to its true moments. The solid curve in the left panel shows the double Gaussian representation of their LOSVD. The dotted curve is the Gauss-Hermite LOSVD of which the true moments best fit those of the double Gaussian LOSVD. This corresponds to the minimum in the goodness-of-fit parameter χ^2, shown in the right panel. The change in grey scale from black to white represents the increase in χ^2, as function of the higher order moments h_3 and h_4, while minimized over the lower-order moments Σ_{GH}, V_{GH} and σ_{GH}. Besides this (global) minimum around $(h_3, h_4) \sim (-0.15, 0.07)$, there are various (broader) local minima. Hence, starting from $(h_3, h_4) = (0, 0)$, a minimization routine easily ends up in e.g. the local minimum around $(h_3, h_4) \sim (-0.05, -0.05)$, resulting in Gauss-Hermite LOSVD indicated by the dashed curve in the left panel.*

then the probability is high that it ends up in one of the (in general broader) local minima. Moreover, since the higher order true moments are sensitive to the wings of the LOSVD, small (numerical) errors in the true moments can lead to (very) wrong estimates of Gauss-Hermite moments. Instead of fitting directly the true moments, an alternative method is to (re)construct the LOSVD from the true moments and then fit a Gauss-Hermite series to it.

For the (re)construction of the LOSVD from the true velocity moments, one can use the well-known Gram-Charlier series, the terms of which are simple functions of the true moments (see e.g. Appendix B2 of van der Marel & Franx 1993), but it has poor convergence properties. The terms in the Edgeworth (1905) expansion are also directly related to the true moments, but since it is a true asymptotic expansion its accuracy is controlled, so that, unlike the Gauss-Hermite and Gram-Charlier expansions, convergence plays no role (see Blinnikov & Moessner 1998 for a comparison between the expansions and for further references).

The Edgeworth expansion of the LOSVD up to order N is given by

$$\mathcal{L}_N^{\mathrm{ED}}(v) = \Sigma \frac{e^{-\frac{1}{2}w^2}}{\sqrt{2\pi}\sigma} \left[1 + \sum_{n=3}^{N} D_n \right], \tag{C.1}$$
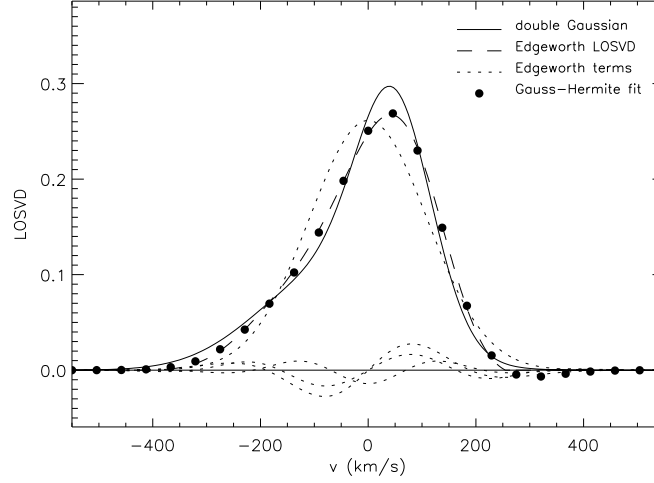
FIGURE C.2 — *Derivation of the Gauss-Hermite moments of the Scorza & Bender (1995) double Gaussian LOSVD (solid curve) by fitting to the reconstructed Edgeworth LOSVD (dashed curve) from its true moments. The Gaussian and the higher order terms of the Edgeworth expansion (C.1) are shown by the dotted curves. The best-fit Gauss-Hermite LOSVD to the Edgeworth LOSVD is indicated by the filled circles.*

with $w = (v - V)/\sigma$ and

$$D_n = \sum_{\{l_{i-2}\}} \mathcal{H}_{n+2(l-1)}(w) \prod_{i=3}^{n} \frac{1}{l_{i-2}!} \left(\frac{d_i}{i!} \right)^{l_{i-2}} . \tag{C.2}$$

The Hermite polynomials $\mathcal{H}_m$ are related to those defined by van der Marel & Franx (1993) as $\mathcal{H}_m(w) = \sqrt{m!}\, H_m(w/\sqrt{2})$. We have defined $l = \sum_{j=1}^{n-2} l_j$, where the sets $\{l_j\}$ are the non-negative integer solutions of the Diophantine equation $l_j + 2l_j + \cdots + (n-2)l_{n-2} = n - 2$. Substituting these solutions, we find up to order $N = 5$

$$\mathcal{L}_5^{\rm ED}(v)\Sigma \frac{e^{-\frac{1}{2}w^2}}{\sqrt{2\pi}\sigma} \left[1 + \mathcal{H}_3(w)\frac{d_3}{3!} + \mathcal{H}_4(w)\frac{d_4}{4!} + \mathcal{H}_6(w)\frac{1}{2}\left(\frac{d_3}{3!}\right)^2 \right.$$
$$\left. + \mathcal{H}_5(w)\frac{d_5}{5!} + \mathcal{H}_7(w)\frac{d_3}{3!}\frac{d_4}{4!} + \mathcal{H}_9(w)\frac{1}{6}\left(\frac{d_3}{3!}\right)^3 \right]. \tag{C.3}$$

The lower-order moments Σ, V and σ are equivalent to those in eq. (3.13), while the higher-order moments d_i $(i \geq 3)$ are cumulants of the true moments

$$d_i = \frac{i!}{\sigma^n} \sum_{\{l_k\}} (-1)^{l-1}(l-1)! \prod_{k=1}^{i} \frac{1}{l_k!} \left(\frac{\mu_k}{k!} \right)^{l_k}, \tag{C.4}$$

so that

$$d_3 = \xi_1, \quad d_4 = \xi_2 - 3, \quad \text{and} \quad d_5 = \xi_3 - 10\xi_1. \tag{C.5}$$

The central moments ξ_1 (skewness), ξ_2 (kurtosis) and ξ_3 are related to the true moments respectively as

$$
\begin{aligned}
(\mu_0\sigma)^3\,\xi_1 &= \mu_0^2\,\mu_3 - 3\,\mu_0\,\mu_1\,\mu_2 + 2\,\mu_1^3, & \text{(C.6)} \\
(\mu_0\sigma)^4\,\xi_2 &= \mu_0^3\,\mu_4 - 4\,\mu_0^2\,\mu_1\,\mu_3 + 6\,\mu_0\,\mu_1^2\,\mu_2 - 3\,\mu_1^4, & \text{(C.7)} \\
(\mu_0\sigma)^5\,\xi_3 &= \mu_0^4\,\mu_5 - 5\,\mu_0^3\,\mu_1\,\mu_4 + 10\,\mu_0^2\,\mu_1^2\,\mu_3 - 10\,\mu_0\,\mu_1^3\,\mu_2 + 4\,\mu_1^5. & \text{(C.8)}
\end{aligned}
$$

Substituting the line-of-sight true moments μ_k for $k = 0, \ldots, K$, we can compute $\mathcal{L}_K^{\mathrm{ED}}(v)$ at each position on the plane of the sky. By fitting a Gauss-Hermite series to $\mathcal{L}_K^{\mathrm{ED}}(v)$, we then obtain the observables Σ_{GH}, V_{GH}, σ_{GH} and higher order moments h_3, h_4, ..., as function of (x', y'). This method (Fig. C.2) is more accurate (and faster) than fitting the true moments directly. Still, (numerical) errors in the higher order moments might result in large (nonphysical) fluctuations in the reconstructed LOSVD. To avoid this we truncate the expansion when higher order terms exceed the lower order terms. Tests reveal that the truncation only happens in a few cases, when the Gauss-Hermite moments reach unrealistic large values.